81-2-153

DEUTSCHES ELEKTRONEN-SYNCHROTRON DESY

DESY 80/128
December 1980

C E L L O - A NEW DETECTOR AT PETRA

CELLO Collaboration

presented by Mina-Jacqueline Schachter

NOTKESTRASSE 85 · 2 HAMBURG 52

To be sure that your preprints are promptly included in the
HIGH ENERGY PHYSICS INDEX ,
send them to the following address (if possible by air mail) :

DESY
Bibliothek
Notkestrasse 85
2 Hamburg 52
Germany

DESY 80/128
December 1980

C E L L O - A NEW DETECTOR AT PETRA

CELLO Collaboration

Deutsches Elektronen-Synchrotron, Hamburg
Kernforschungszentrum und Universität+, Karlsruhe
Max-Planck-Institut für Physik und Astrophysik+, München
Laboratoire de l'Accélérateur Linéaire, Orsay
LPNHE, Paris
Centre d'Etudes Nucléaires, Saclay

Presented by
Mina-Jacqueline Schachter

Contributed paper to the International Conference on Experimentation at LEP - University of Uppsala, Sweden, June 16-20, 1980

+) Supported by Deutsches Bundesministerium für Forschung und Technologie

A b s t r a c t

A description of the design characteristics of CELLO, a large 4 π magnetic detector at PETRA, is given and first results of beam operation are presented.

C E L L O C o l l a b o r a t i o n
presented by Mina-Jacqueline Schachter

H.-J. Behrend, J. Field, V. Schröder, H. Sindt,
Deutsches Elektronen-Synchrotron, Hamburg

W.-D. Apel, J. Bodenkamp, D. Chrobaczek, J. Engler, D.C. Fries, G. Flügge, H. Müller, H. Randoll, G. Schmidt, H. Schneider,
Kernforschungszentrum und Universität, Karlsruhe

W. de Boer, G. Buschhorn, G. Grindhammer, P. Grosse-Wiesmann, B. Gunderson, C. Kiesling, R. Kotthaus, H. Lierl, D. Lüers, T. Meyer, L. Moss, H. Oberlack, P. Schacht, M.-J. Schachter, A. Snyder, H. Steiner+,
Max-Planck-Institut für Physik und Astrophysik, München

G. Carnesecchi, A. Cordier, M. Davier, D. Fournier, J.F. Grivaz, J. Haissinski, V. Journé, F. Laplanche, F. Le Diberder, J.-J. Veillet, A. Weitsch,
Laboratoire de l'Accélérateur Linéaire, Orsay

R. George, M. Goldberg, B. Grossetête, F. Kapusta, F. Kovacs, G. London, L. Poggioli, M. Rivoal,
LPNHE, Paris

R. Aleksan, J. Bouchez, G. Cozzika, Y. Ducros, A. Gaidot, J. Pamela, J.P. Pansart, F. Pierre,
Centre d'Etudes Nucléaires, Saclay

+) Alexander von Humboldt Foundation Senior American Scientist
University of California, Berkeley, Ca.

C o n t e n t s

1. Introduction

2. Central tracking detector

2.1 Cylindrical proportional wire chambers

2.2 Cylindrical drift chambers

2.3 End cap proportional wire chambers

3. Lead liquid argon calorimeter

3.1 Structure and wiring of the central calorimeter

3.2 Structure and wiring of the end cap calorimeter

3.3 Electronics and signal processing

3.4 Performance of the calorimeter

4. Muon detector

5. Forward detector

6. Trigger system

6.1 Charged particle trigger

6.2 Neutral particle trigger

7. Data acquisition

8. Event reconstruction and physics analysis

9. Summary

1. Introduction

CELLO[1] is a general purpose magnetic detector operating at PETRA since March of 1980 at center of mass energies around 35 GeV. The analysis of high energy e^+e^--collisions demands complete detection and identification of leptons and hadrons. CELLO is optimized for electron and photon detection at the expense of extensive particle identification.

A schematic view of the CELLO detector is shown in Fig. 1. The compact tracking detector consisting of proportional and drift chambers is mounted inside a superconducting solenoid of 80 cm radius producing an axial field of 1.3 T. The high current density superconducting coil of novel design[2] has a wall thickness of only 0.5 radiation length (X_0) including cryostat and insulating material and thus does not seriously interfere with the detection of electrons and photons in a fine grain lead liquid argon calorimeter outside the coil. The iron return yoke of the magnet serves as a hadron absorber behind which muons are detected in planar proportional wire chambers covering an area of about 200 m^2. Forward spectrometers consisting of drift chambers, scintillation counters and lead-glass shower counters are used to tag two-photon collisions and to measure small angle Bhabha scattering for luminosity determination. Table I summarizes important parameters of the various detector components.

This paper describes the individual detector elements, the trigger and data acquisition schemes and gives an account of the detector performance in tests and under beam conditions.

2. Central Tracking Detector

The central detector is required to

- operate in an axial magnetic field up to 1.5 T
- provide accurate position determination in the axial (z) direction for tracking and the azimuthal (ϕ) direction for tracking and momentum determination
- have good coordinate correlation for reconstructing space points to achieve high resolving power for nearby tracks in multiparticle jet events
- provide a fast charged particle trigger in less than 2 μs using information from both rφ- und rz-projections.

Cylindrical proportional wire chambers (PWC) interleaved with drift chambers (DC) concentric with respect to the beam axis have been chosen to fulfill these requirements (Fig. 2). There are 5 PWCs, each having axial anode wires and 2 cylindrical cathodes finely segmented in strips oriented at 90^0 and 30^0 with respect to the cylinder axis. The cathode strips are equipped with analog readout and provide very accurate z determination. Pulse height correlation between the induced signals on the 90^0 and 30^0 cathode strips facilitate the reconstruction of space points.

7 cylindrical layers of drift chambers allow for a precise position measurement in the plane of magnetic deflection (rφ plane).

All 5 PWCs and 2 DCs are used to derive a charged particle trigger.

Table II summarizes the relevant parameters of the cylindrical tracking device. The anode wire layers are arranged at radii between 17 and 70 cm thus resulting in a visible radial track length of 53 cm. The wire length is 220 cm for all chambers. The solid angle covered by at least 8 wire layers is $.91 \times 4\pi$.

2.1 Cylindrical Proportional Wire Chambers

The main characteristics of CELLO's proportional chamber system are:

- charge measurement on the cathodes in order to get a good precision on the longitudinal coordinate z and an efficient track separation in high multiplicity events

Table I: Characteristics of the CELLO detector

Detector component	Number of modules	Solid angle ($\Delta\Omega/4\pi$)	Typical dimensions (cm)	Important Properties
Tracking device	5 cyl. PWCs 7 cyl. DCs	0.91	length = 220 radius = 17-70	σ_z = 440μ, charge measurement on cathodes $\sigma_{r\phi}$ = 170
	8 plan.PWCs	0.10	radius = 21-66	semicircular shape
Central solenoid	1		length = 400 radius = 80	superconducting, up to 1.3 T thickness = .49 X_0
Compensating solenoid	2			superconducting, up to 3.5 T
Liquid argon shower detectors	16 cyl. 4 end caps	0.96		$\sigma_e(E)/E = .085/(E(GeV))^{1/2}$* angular resolution 4 mrad typ.
μ-chambers	32	0.92	200x300 to 300x400	σ = ± 6 mm correlated space points by cathode readout
Forward detectors	24 DCs 96 scint. 112 Pb-gl.	25mr≤ Θ≤50mr 0≤φ≤2π		σ = 300μ $\sigma_e(E)/E = .05/(E(GeV))^{1/2}$* probability of misidentifying a hadron as electron ≤ 2% down to 2 GeV

*): As obtained from tests of prototype modules

- use of cathodes perpendicular to the anode wires, which provide the information in the z-coordinate to the trigger.

The anode wire spacing of the five PWCs varies between 2.09 and 2.86 mm (see Table II). There is a total of 5120 wires, their diameter is 20 μm. The gap width is 2 x 4 mm. The spatial resolution averaged over all chambers is $\sigma_{r\phi}$ = 0.24 x wire spacing, consistent with the theoretical expectation.

To achieve the best resolution of the longitudinal coordinate z one set of cathode strips is chosen to be annular. Their width is of the order 4.5 mm. To optimize the orientation of the other cathodes two constraints have been taken into account:

- the angle between cathodes and anodes should be approximately 45^0 to resolve coordinate ambiguities
- the cathode helix should not run through a full circle.

The angle chosen is 30^0. The cathodes were mechanically realized by free standing mylar cylinders with strips of silver paint. The precision of the position determination in the longitudinal direction is on the average σ_z = 440 μm[3] (Fig. 3). The corresponding variation as a function of the angle of incidence of the track is shown in Fig. 4.

Analog measurement of the induced charge collected on the strips is done for each of the 4400 channels. In order to disentangle overlapping cathode clusters from different tracks the charge correlation between 30^0- and 90^0-cathodes is used. The ratio

$R = \frac{q_{30^0}}{q_{90^0}}$ depends on the location of the individual anode wires between inner and outer cathode cylinders. Therefore for each chamber and appropriate surface regions this ratio is calibrated (Fig. 5). A single space point can be reconstructed with an accuracy of $\sigma_{r\phi} \cdot \sigma_z = (0.5\ \text{mm})^2$ using both cathodes and the anode wires.

2.2 Cylindrical Drift Chambers

An entirely open drift cell structure has been chosen[4, 5]. This keeps the number of potential wires at a minimum. The drift cells are arranged on cylindrical surfaces (see Table II). Adjacent sense wires are separated electrostatically by a triplet of potential wires (Fig. 6).

There are no further field shaping electrodes. A similar cell structure was first used in the MARK II detector[6] at SPEAR. The design aims at a simplified construction, high reliability for remote operation, and a low density active volume unobscured by structural material to reduce multiple Coulomb scattering as much as possible. The small cell width of about 15 mm (see Table II) is dictated by the strong axial B-field and the required double track resolution for jet events with high local track density. 'Single hit' electronics is used with an amplifier/discriminator hybrid directly mounted on the chamber and a TDC which consists of a low noise sample and hold amplifier and an 8-bit ADC to digitize a maximum time interval of 810 ns. A gas mixture of 90% Ar and 10% Methane is used.

The uncompensated Lorentz force of the strong transverse B-field on the drifting electrons causes substantial drift path distortions. Fig. 7a shows drift trajectories calculated for B = 1.5 T and various angles of incidence. The measured space time relation at B = 1.43 T for tracks of normal incidence and inclined by + 30^0 with respect to the normal are shown in Fig. 7b. For moderate distances from the sense wire drift times for positive and negative angles of incidence are similar. For tracks passing through the edges of a cell there are substantial drift time differences for oppositely inclined tracks causing a large ± asymmetry. The observed nonlinearities and angular dependencies can be very accurately parametrized using a computer simulation of the drift process in inhomogenous E- and B-fields[5]. Fig. 8a shows the distribution of residuals of fitted tracks of cosmic rays as a function of the position in the cell as measured at B = 1.3 T for angles of incidence up to 30^0. The data still show some systematic variations which are also reflected by the non-Gaussian tails of the projected distribution (Fig. 8b). A recent determination of the resolution using Bhabha scattering events and more refined conversion constants results in 170 μ r.m.s. (Fig. 9). The local precision not averaged over the whole drift cell and all angles of incidence is better than 100μ. This demonstrates that the spatial accuracy is dominated by systematic uncertainties like quantization of time digitization (3.2 ns), wire displacement due to gravitational and electrostatic forces, and alignment errors.

Table II: Layer structure of central tracking device

Layer	Type	Radius (cm)	# of anode wires, drift cells	wire spacing, drift cell width (mm)	# of cathodes 90°	30°
1	PC	17.0	512	2.09	252	256
2	PC	21.0	512	2.58	228	256
3	DC	25.5	104	15.41	---	
4	DC	30.4	128	14.92	---	
5	PC	35.7	1024	2.19	366	512
6	DC	40.2	168	15.03	---	
7	DC	45.1	192	14.76	---	
8	DC	50.0	208	15.10	---	
9	PC	55.3	1536	2.26	420	768
10	DC	59.8	256	14.68	---	
11	DC	64.7	256	15.88	---	
12	PC	70.0	1536	2.86	494	768

2.3 End Cap Proportional Wire Chambers

The end cap multiwire proportional chambers of the CELLO detector are placed at the ends of the cylindrical part of the central tracking device. They cover the acceptance region of $153 < \Theta < 428$ mrad.

The system consists of four identical planar units, semicircular in outline. At each end, two of the units are attached to the front of one of the liquid argon end cap cryostats so that they form a circular disk normal to the PETRA beam axis. Fig. 10 shows a schematic view of the layout of one half of a chamber unit.

Each unit consists of two electrically separated chambers which are glued together at two of their cathode planes. One chamber of each unit is at $z = \pm 1405$ mm with wires oriented parallel to the x-axis (so these chambers measure the y-coordinate), and the other chamber is at $z = \pm 1425$ mm with a wire orientation to measure the x-coordinate.

The induced charge on the cathodes of the chambers is measured digitally. One of the cathode planes of each chamber is divided into equally sized sectors each representing a $\Delta\phi$ of $180^{\circ}/32$. The other cathode plane of each chamber is divided into concentric rings. Each ring covers an interval in Θ equal to the interval of a 90° cathode strip of the central detector.

3. Lead Liquid Argon Calorimeter

The dominant design considerations for the electromagnetic calorimeter have been good electron-hadron separation and good detection efficiency, energy resolution and spatial resolution for low energy photons over the entire solid angle. These requirements are fulfilled by a barrel shaped lead liquid argon calorimeter with end caps.

The cryogenic system has to supply three cryostats filled with liquid argon (Fig. 1):

- One cylindrical cryostat of 25 m^3 volume contains 2 x 8 separate modules (stacks). The stacks are arranged mirror symmetric with respect to the $z = 0$ plane and form an octagonal symmetry in ϕ.
- Each of the two symmetric end cap cryostats contains two half cylindrical stacks.

3.1 Structure and Wiring of the Central Calorimeter

Each of the 16 stacks has a trapezoidal cross section corresponding to a sector of an octagon with a length of 2 m, and a width of 85 cm in the first and 121 cm in the last layer (Fig. 11a). In depth the stack measures 43 cm which is equivalent to 20 radiation lengths. This is large enough to contain fully an electromagnetic shower even at the largest PETRA energies.

To obtain good spatial resolution we have adopted a layer scheme of lead strips (1.20 mm thick) alternating with continuous lead plates (also 1.20 mm thick). The gap width is 3.6 mm. The strips are held at a positive high voltage relative to the plates. The orientations of the strips are defined, such that there is a configuration of phi-measuring (i.e. 0^0 to the beam axis), theta measuring (90^0) and diagonal (45^0) strips. The 0^0- and 90^0-strips are 2.3 cm wide, whereas the 45^0-strips are 3.25 cm wide. The lateral segmentation is matched to the transverse shower dimension. In front of each stack there are two additional layers which serve as dE/dx gaps. These layers are built of copper foils glued on epoxy plates (Fig. 11a) with a gap width of 6 mm.

In order to avoid structural material in front of the calorimeter and to minimize gaps between adjacent stacks, the lead modules are mainly supported from the rear. This demands a very solid construction to avoid a sagging of the lead beyond the expected setting point. The overall dead area of the stacks amounts to less than 3.5% of the total solid angle.

A wiring scheme has been chosen that allows optimum resolution in space while simultaneously keeping down the number of electronic channels to 384 per stack. The strips are grouped laterally to 20 mrad bins. For directions approximately perpendicular to the beam axis, every single strip is read out, while for smaller polar angles strips are electrically combined. The number of electronic channels is reduced even further without degrading the local resolution by connecting together widely separated strips in the same layer. Clearly a fine position measurement is not needed deep inside the shower detector. Here a coarser grouping of strips is used. In view of good π/e separation 6 independent samplings in depth are taken for each strip orientation.

3.2 Structure and Wiring of the End Cap Calorimeter

Each module in the end cap part consists of 42 layers of lead strips interleaved with full plates. The strips are alternately vertical, horizontal and circular (Fig. 11b). The lead thickness is 1.2 mm and the argon gap 4 mm. The radial extension of the lead stacks in the end caps is from 23 to 66 cm ($5^0 < \Theta < 30^0$). In front of the lead calorimeter are 3 planes of copper foils glued on epoxy for dE/dx measurement. The total thickness of the detector is 21 radiation lengths. The detector is built in such a way that corresponding strips form sectors pointing to the interaction region. The number of electronic channels is 368 per module.

3.3 Electronics and Signal Processing

There is a total of 8000 electronic channels in the lead liquid argon calorimeter. The analog signals are processed by a preamplifier with 4 channels on a board, directly attached to the cryostat. The signals are transmitted to the counting room by a twisted pair cable and fed into the main amplifier with 16 channels on a board. Digitizing takes place in a sample-and-hold circuit and a comparator which compares the pulse with a staircase voltage function generated for 64 channels simultaneously. The final data handling is organized on a readout card where channels with signals below a certain noise level can be suppressed. The electronic noise distribution as a function of the channel capacities is shown in Fig. 12. Minimum ionizing particles deposit a charge of 5.2 fc/per double gap. This is about 4 times larger than the noise in the low capacity (double gap) channels. For high capacity channels where several gaps are connected together the situation is even more favourable. Thus minimum ionizing particles can be safely detected.

3.4 Performance of the Calorimeter

Before installation at CELLO one full size stack was tested[7] in a hadron/electron beam at CERN and in an electron/photon beam at DESY. The energy resolution measured in these tests was degraded by material in front of the calorimeter (0.6 X_0 at CERN and 1.0 X_0 at DESY). The resolution obtained by

extrapolating to zero material is $\sigma_E/E = 0.085/(E(Gev))^{1/2}$. Fig. 13a shows preliminary data on the energy distribution of Bhabha events selected by triggering on the energy deposition in the central liquid argon calorimeter. The width of the distribution is largely due to the still incomplete calibration of individual channels. Fig. 13b displays the energy resolution (σ_E/E) as function of the energy for the CERN test data together with the value obtained for the Bhabha events at the highest PETRA energy (18.25 GeV).

The reconstruction of showers from 1 GeV electrons determines the center of a shower with an overall resolution of $\sigma = \pm$ 3 mm. Spatial resolution for the end cap calorimeter has been measured by selected Bhabha events. The radius found from hits in the vertical and horizontal strips is compared with the radius from the semicircular strips (Fig. 14). The resolution is about 5 mm for 2 cm strips.

The pion-proton separation using ionization measurement was studied for the CERN data. The charge distribution for 1 GeV protons and pions for a given dE/dx channel are shown in Fig. 15. For this channel (single gap) we obtain a π/p separation efficiency of 76%.

The first performance test of the whole liquid argon detector is provided by the measurement of the angular distribution of Bhabha events. The preliminary distribution follows the QED-prediction (Fig. 16a) normalized to the end cap Bhabhas. The number of Bhabhas agrees well with the luminosity obtained from the forward detector. The angular distribution for $e^+e^- \rightarrow \gamma\gamma$, triggered and selected only by means of the calorimeter information, is displayed in Fig. 16b.

4. Muon Detector

The 32 muon chambers, in 3 sizes ranging from 2 x 3 m^2 to 3 x 4 m^2, are at about 3 meters from the interaction region and cover a total area of about 200 m^2.

The iron return yoke of the magnet, just in front of the chambers, serves as a hadron filter of 5-8 absorption lengths. Due to the multiple scattering of the muons in the iron filter a precision of only $\pm$ 1 cm is required. Thus, muon detection requires large chambers with rather limited precision. In order to get a good rejection of hadron contamination the two coordinates have to be measured without ambiguity. To keep the number of channels

moderate, the chambers have a drift cell structure but are read out as proportional chambers.

The anode wire spacing of the chambers is 12.7 mm, the anode wires are separated by one field wire. The gap width is 2 x 8 mm. The cathodes are made of 10.6 mm wide copper foil strips on mylar. They are glued on a honeycomb structure of 6 cm thickness (Fig. 17). The orientation of the cathode strips is $\pm$ 34.27^0 with respect to the anode wires. The reconstruction of a hit in the chamber is possible without ambiguity using the anode wires and the two cathode strip planes. For the normal high voltage setting a track hit gives an induced charge distribution over 3-4 strips. As the charge on the strips is not measured, the geometrical center of the cluster is taken.

The precision of the reconstructed hit is $\pm$ 6 mm in the x direction perpendicular to the anode wires. The precision of the y coordinate in the direction of the anode wire is also about $\pm$ 6 mm. The accuracy of the y determination comes from the DISTY distribution shown in Fig. 18. DISTY is the distance along the anode wire between the intersections of the geometrical centers of the clusters from the two cathodes as indicated in the insert of Fig. 18.

From data taken in a cosmic ray run, the difference in both projections between the hits in the muon chambers and the expected points obtained after reconstructing the tracks in the central detector is calculated and shown in Fig. 19. The σ of about 4 cm is compatible with that expected taking into account multiple scattering of 2-5 GeV cosmic rays in the iron and in the lead stacks.

5. Forward Detector

The forward detector arms are able to measure and identify electrons in the angular region from 25 mrad to 50 mrad. The electron tagging at small angles monitors the luminosity based on Bhabha events and helps analyse two photon events. The detector consists of drift chambers, scintillators and lead glass blocks which have to stand a high background of synchrotron radiation and beam gas interaction.

Each quarter of the detector is mounted on pivoting supports and contains three groups of two planar drift chambers, each with 11 sense wires oriented at 45^0 and 135^0 with respect to the vertical. The major parameters

of the drift chambers are: diameter of sense wires 20 μm, distance between sense wires 44 mm, gap width 2 x 5 mm, fieldshaping cathodes with 100 μm wires, and a 30% isobutane/70% argon gas mixture. Because of the high background, multihit TDCs are used with 4 ns least count error. Large scintillators cover the active area of the drift chambers in the first and third group. The middle group contains two planes of 12 overlapping finger scintillators each 66 mm wide. They help to resolve the left-right ambiguity and exclude synchrotron radiation hits from trackfinding. Track localization is possible in an area of 48 x 52 cm^2. Reconstructed cosmic rays in the drift chambers measure a spatial resolution of σ = 300 μm (Fig. 20).

The last element in each arm is a lead glass shower counter consisting of 6 vertical, 6 horizontal and 16 longitudinal blocks with thicknesses of 3, 3, 14 radiation length. The energy resolution of the lead glass calorimeter far from the beam pipe is $\sigma(E)/E = 0.05/(E(GeV))^{1/2}$. Using the pulse heights in the three layers it is then possible to make cuts on the data so that only 2-3% of minimum ionizing particles are misidentified as electrons.

Three processes can be triggered on using the forward detector: e^+e^-, $\gamma\gamma$, e^+e^-X. The Bhabha trigger requirement is that collinear forward and backward quarters of lead glass counters give a high signal in coincidence with hits in the corresponding scintillator hodoscope elements. For the $\gamma\gamma$ final state an anti-coincidence with the scintillators is required. The double electron tagging is similar to the Bhabha trigger except that one electron must have low energy. A single tagging signal to be used in coincidence with signals from other CELLO detector components is also available.

6. Trigger System

The trigger system consists of three elements: charged particle triggers from the tracking device, energy triggers from the liquid argon calorimeters, and energy triggers from the forward detector lead glass counters (Fig. 21). Different combinations of these triggers can be selected under computer control.

6.1 Charged Particle Trigger

The charged particle trigger is a software programmable hardware track finding processor acting on the chamber signals after each bunch crossing. Its inputs are the signals from the anodes and 90^0 cathodes of the five proportional chambers and from two layers of the drift chambers in the cylindrical part of the tracking device.

A fast decision is taken in less than 1500 ns on the basis of following requirements:

1) Curved tracks in the rϕ projection above a preselected transverse momentum (typically 350 MeV/c) are found from the anode wires of the proportional chambers and the drift cells.

2) Straight tracks are found in the rz projection within a limited region around the interaction point from the 90^0 cathodes of the proportional chambers.

The chamber signals are grouped in 64 azimuthal and 37 polar sectors. The sector signals are fed to the address lines of Random Access Memories (RAMs), in which masks of all allowed tracks are stored. Whenever a certain pattern on the RAM address lines coincides with a valid mask, the appropriate memory position generates a logic "one" in the output line of the RAM. The precomputed valid mask patterns are loaded at the beginning of the experiment into the RAMs.

A summation logic counts the total number of masks which are hit and compares it with a software preselected trigger condition. Each mask is assigned a reference sector corresponding to the hit in the outermost layer of the tracking device. The trigger condition can also be defined by a preselected number of reference sectors. If the trigger condition in both projections is fulfilled, an interrupt signal is fed to the computer for starting the readout process. Usually the trigger condition r$\phi(\geq 2$ sectors) $\cdot$ rz$(\geq 1$ sector) was used. In addition there is a signal generated for r$\phi(\geq 1$ sector) $\cdot$ rz$(\geq 1$ sector) which is used for combined triggers with the liquid argon and forward counters.

The system is organized in a total of 64 plus 37 single width CAMAC-modules corresponding to the rϕ- and rz-sectors. All masks contributing to a trigger are stored according to their sector number and shape code and read

out by the computer. This information is used for a fast data reduction. It is possible to obtain a large background reduction factor in the analysis of hadronic events (jets) just by applying certain cuts to the number of masks and their topological configuration.

Four masks are stored in each RAM (1024 x 4 bits). There are 12 RAMs per reference sector so that a total of 48 different shape codes can be stored. The mask finding takes about 600 ns.

Due to the large storage capacity of the RAMs, it was possible to develop a set of masks which allows for chamber inefficiencies. In the $r\phi$ geometry, for example, three different track definitions are used:

a) any five of the seven chambers fired
b) any six fired
c) all seven chambers fired.

Multiple counting of non-overlapping tracks is avoided. The treatment of background hits in the chambers can be varied according to the experimental conditions, i.e. a track plus a neighbouring single hit which could be combined with some of the track hits to a valid mask, gives either two tracks (if this does not increase the trigger rate too much) or one track (the additional hit is treated as background). The system can be tested with patterns generated by a minicomputer (LSI 11). During data taking a continuous monitoring of the system via the minicomputer is done.

6.2 Neutral Particle Trigger

This trigger uses the information on the energy deposition either in the cylindrical or in the end cap liquid argon system. The central argon trigger sums the analog signals of 4 groups of layers in each module to give a representative sampling in depth (Fig. 10). The summed energy is also available for two sets of quadrants. To avoid edge effects the two sets of quadrants are rotated by one module (45^0; Fig. 22). Total forward and backward analog sums are also formed, and finally the sum of the whole system. Using these analog signals with suitable discriminator thresholds different triggers can be formed, either from the liquid argon information alone or in conjunction with the charged trigger. The end cap liquid argon trigger is based on the energy sum per quarter (one module). All signals

from the semicircular strips of a module are added (with the proper weight) and compared to discriminator thresholds. A more restrictive trigger - two and only two modules - is used for online luminosity monitoring. The liquid argon trigger allows for a selection of the Bhabha scatters independent of any track information and facilitates triggering on all neutral final states like $e^+e^- \rightarrow \gamma\gamma$.

7. Data Acquisition

The data acquisition philosophy is to read data via a CAMAC-system and to have dedicated computers distributed over the system in order to supervise the detector and to provide a reliable data path to the DESY computer center. Error recovering, interaction, and status as well as event display facilities are implemented to support the physicist on shift. Fig. 23 shows an overview of the CELLO data acquisition system and the main data flow.

The various CELLO detector components are read out by a CAMAC-ROMULUS[8] system. Each detector and the trigger processor has its own ROMULUS branch assigned. This enables the online computer to collect the data with a minimal overhead (one direct memory access for each detector). To identify the transferred channels in case of suppressed transmission (see 3.3) block address generators (BAG) add address information to every data word. Furthermore individual hardware processors (ax + b units) transform the ADC contents into appropriate physical numbers by a programmable linear transformation.

Each ROMULUS-branch can be read either by one of the two online computers or by a minicomputer which also has access to the same crate dataway. Thus, the minicomputer can calibrate and test its assigned detector without interfering with the rest of the system. During data acquisition of the online computer, the minicomputers also have access to the data stream passing their own crate dataway. They are thus able to monitor the performance of their detector.

The online computers are dedicated to special tasks. The first, a PDP11/45, is responsible for fast event acquisition and averages peak rates by supplying a large buffer. Each event is analysed using the $r\phi$ trigger

information and the anode readout of the proportional chambers. This allows a rough reconstruction of tracks in about 1.5 ms per track. On this basis events are classified according to different physical processes. This takes about 50 ms per event. Presently, all events are sent to the second online computer, a PDP 11/55, via a CAMAC link. Both online computers are equipped with tape drives to which the event stream can be dynamically redirected.

An elaborate dialog task, running on the PDP 11/55, allows the physicist to control the whole experiment. Messages and commands can be distributed to and received from all computers, even down to the minicomputers in the readout system. The physicist can invoke low priority monitor tasks, e.g. an interactive event display. The second online computer passes the events to the DESY-IBM computer triplex.

The IBM online stores the events on a disk file which is organized as a large ring buffer. If the space in this buffer is almost exhausted, a DUMP job is automatically invoked which transfers the data onto tape. This allows the IBM to accept a continuous data flow occupying a tape drive for short time. Data integrity is assured by checking each arriving event and responding with a positive or negative acknowledgment. Some online analysis is done in order to monitor the performance of the detector continuously.

Events classified online as hadronic or QED-events are written onto special disk files on the IBM. Less than 1% are thus selected. They are scanned during the run using an interactive display system. This makes possible a crude determination of the total hadronic cross section shortly after the data are taken.

8. Event Reconstruction and Physics Analysis

In addition to the online selection described above an independent off-line program selects data directly from the dump tapes. Either the filtered samples or the data on the dump tape are then passed to the main reconstruction program, OFFRAM.

OFFRAM consists of a number of semi-independent processors to reconstruct the event and to perform higher level tasks. The order in which the various processors are called and their working parameters are read in at execution time. Since the reconstruction of events is the largest fraction of computing load from CELLO an effort has been made to insure

that all OFFRAM-programs can be run on any of the computer systems available in the collaboration (CDC, IBM, UNIVAC).

The pattern recognition in the inner detector proceeds as follows: Space points are found in the proportional chambers either by correlating the charge deposited on the 90°- and 30°-cathodes of each chamber or by associating anode with cathode hits. In the $r\phi$ projection circular roads are searched for tracks. The ability of the program to reconstruct properly even high multiplicity hadronic events is demonstrated by Fig. 24.

For the liquid argon calorimeter data the pattern recognition program makes use of the known geometrical correlations among the Θ, ϕ and 45° strips in selecting the active channels. Starting from the hits in the three orientations in each of six depth bins, sets of two-dimensional cells are reconstructed which best reproduce the observed hits at each depth. By rejecting uncorrelated hits at this point, the signal to noise ratio is enhanced. The cells are grouped into clusters for each layer in depth. The clusters at different depths are then linked to three dimensional showers. The shower axis is determined by fitting a straight line through the cluster centers. An analysis of Bhabha events shows that we can achieve an angular resolution for the reconstructed shower of 4 mrad.

The output from OFFRAM contains for each event a description of each track and each vertex, intermediate information from the various processors and the raw data itself, in order to permit reprocessing by OFFRAM.

The first analysis reveals the expected results. Two hadronic events are shown in Figs. 24 and 25. A characteristic two jet structure is clearly visible in Fig. 25 which displays a hadronic event at $E_{cm} \simeq 35$ GeV. Some preliminary results concerning the topological properties of hadronic events at $E_{cm} \simeq 35$ GeV are given in Figs. 26 and 27. The sphericity plot in Fig. 26 shows the prominent low sphericity associated with two jet events and the Q-plot[9] of Fig. 27 reveals the existence of planar events with large sphericity.

9. Summary

The CELLO detector is operating successfully at highest PETRA energies. Cylindrical wire chambers are used for charged particle tracking and momentum measurement inside a strong axial magnetic field (B = 1.3 T). The tracking detector has a high resolving power for multiparticle jet events and allows precision measurement of the azimuthal coordinate ($\sigma_{r\phi}$ = 170 μm achieved with drift time measurement) as well as the axial coordinate (σ_z = 440 μm achieved with analog readout of annular cathodes). The thin superconducting coil of novel design works reliably. The lead liquid argon calorimeter, with an acceptance of 0.96 x 4π, has been successfully tested in the first round of data taking using QED processes. The programmable trigger allows low rate triggering with fast online feedback on hadronic and QED events. Results of preliminary data analysis show that the full system is functioning well.

Acknowledgment

We acknowledge the invaluable cooperation of all engineers and technicians at the collaborating institutions. We would like to thank the PETRA machine group for their tremendous efforts in making this experiment possible. The non-DESY members wish to thank the DESY Directorate for the hospitality extended to them.

I would like to thank all the members of CELLO, who have helped in assembling this report by providing material and by discussions.

Figure Captions

Fig. 1 Schematic view of the CELLO detector

Fig. 2 Layer structure of the central tracking detector of CELLO

Fig. 3 Distribution of ($z_{90^o} - z_{track}$) in a PWC of the central tracking detector

Fig. 4 Precision of z as function of the angle of incidence (Θ) of a track

Fig. 5 Charge correlation in one region of a PWC of the central tracking detector. Details are given in the text.

Fig. 6 Drift cell geometry (a) and electric field distribution (b) inside a drift cell

Fig. 7a Contours of equal drift time (solid curves) and lines of force (dashed curves) for 2 adjacent drift cells at B = 1.5 T. The drift time contours are separated by 40 ns. Also indicated are tracks of different angles of incidence and the corresponding paths of shortest drift time

Fig. 7b Space time relation at B = 1.43 T for tracks normal (0^o) to the wire layer and inclined by $\pm 30^o$

Fig. 8 Distribution of residuals of cosmic ray tracks for B = 1.3 T and angles of incidence up to 30^o

a) as a function of the distance from anode wire

b) summed over the whole drift cell

Fig. 9 Same as Fig. 8b for electron tracks from Bhabha scattering at E_{cm} = 35 GeV

Fig. 10 Layout of the end cap proportional wire chambers

Fig. 11 Layout of the lead liquid argon calorimeter

Fig. 11a Structure of a stack in the central liquid argon calorimeter and grouping of strips inside a stack for the neutral trigger

Fig. 11b Orientation of the strips in an end cap liquid argon calorimeter module

Fig. 12 Electronic noise distribution as function of the channel capacities in a central calorimeter stack

Fig. 13 Energy resolution of the lead liquid argon calorimeter

a) Energy distribution of Bhabha events at E_{cm} = 33.8 GeV

b) Energy resolution in the central calorimeter

Fig. 14 Spatial resolution in the end cap calorimeter

Fig. 15 Charge distribution from a dE/dx measurement in one liquid argon layer (CERN test)

a) for 1 GeV protons

b) for 1 GeV pions

Fig. 16 Angular distributions as measured by the calorimeter system

a) for $e^+e^- \to e^+e^-$

b) for $e^+e^- \to \gamma\gamma$

Fig. 17 Structure of a muon chamber

Fig. 18 Precision of the coordinate along the anode wires of the muon chambers

Fig. 19 Residuals of x- and y-coordinates in a muon chamber

Fig. 20 Spatial resolution of the drift chambers in the forward detector

Fig. 21 Block diagram of overall trigger logic

Fig. 22 Grouping of the central calorimeter stacks into two sets of quadrants for the neutral trigger

Fig. 23 Data acquisition system: Hardware configuration and data flow diagram

Fig. 24 Reconstructed charged particle tracks in a high multiplicity annihilation event at E_{cm} = 35 GeV

Fig. 25 Hadronic two jet event at $E_{cm} \gtrsim 35$ GeV. A clear two jet structure is seen in the distribution of charged particle tracks and neutral energy as well

Fig. 26 Sphericity[9] distribution of hadronic events at $\langle E_{cm} \rangle$ = 35.16 GeV
($S = 3/2\ (\Sigma p_T^2)/\Sigma p^2$)

Fig. 27 Distribution of hadronic events in a Q-plot[9] at $\langle E_{cm} \rangle$ = 35.16
$Q_i = \lambda_i/\Sigma p^2$, where λ_i are the eigen values of the momentum tensor $M_{ik} = \Sigma \vec{p}_i \cdot \vec{p}_k$ (i, k = 1, 2, 3). Two jet events cluster at small sphericity $S = 3/2\ (Q_1 + Q_2)$. Planar events are distributed along the edge of low aplanarity $A = 3/2\ Q_1$.

References

1) Proposal for a 4π magnetic detector for PETRA
C E L L O
DESY-Karlsruhe-München-Orsay-Paris-Saclay Collaboration

2) H. Desportes et al., Construction and Test of the CELLO thin wall solenoid
Contribution to the 21st Cryogenic Engineering Conference, Madison, Wisconsin, August 21-24, 1979

3) M. Cohen, Etude des performances des chambres proportionnelles du détecteur central de CELLO, Thèse 3ème cycle LAL-80/10 (unpublished)

4) W. de Boer et al., Nucl. Instr. and Meth. 156 (1978), 249

5) W. de Boer et al., MPI-PAE/Exp El 84

6) W. Davies-White et al., Nucl. Instr. and Meth. 160 (1979), 227

7) W.-D. Apel et al., Test of a module for the CELLO liquid argon calorimeter
to be submitted to Nucl. Instr. and Meth.

8) C. Jacobs, L. McCulloch, CERN CAMAC Note 63-00, September 1976

9) J. D. Bjorken and S. J. Brodsky, Phys. Rev. D1, 1416 (1970)
G. Alexander, XIX Int. Conf. on HEP, Tokyo, 1978
S. L. Wu and G. Zobernig, Z. Physik C2, 107 (1979)

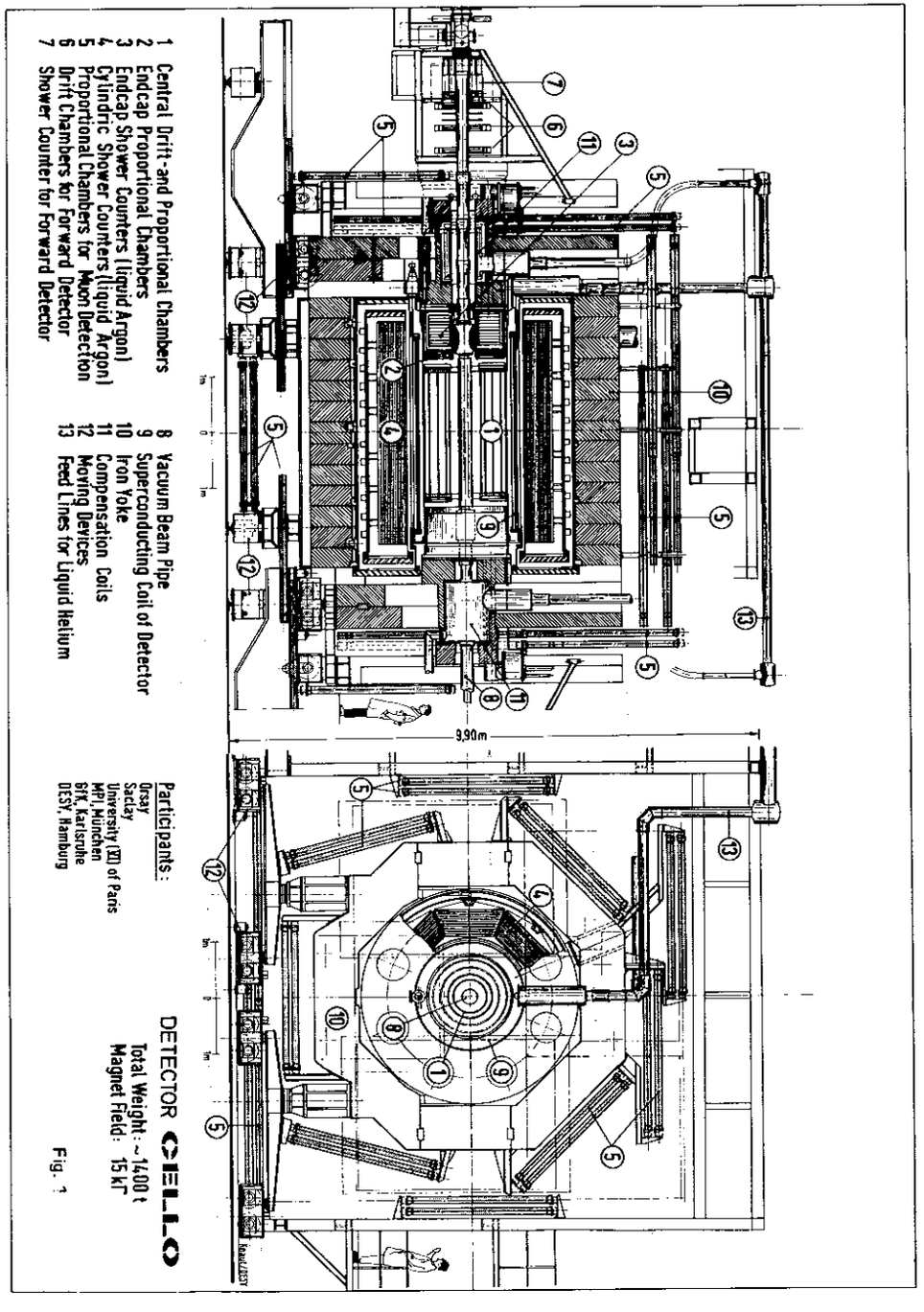

Fig. 1

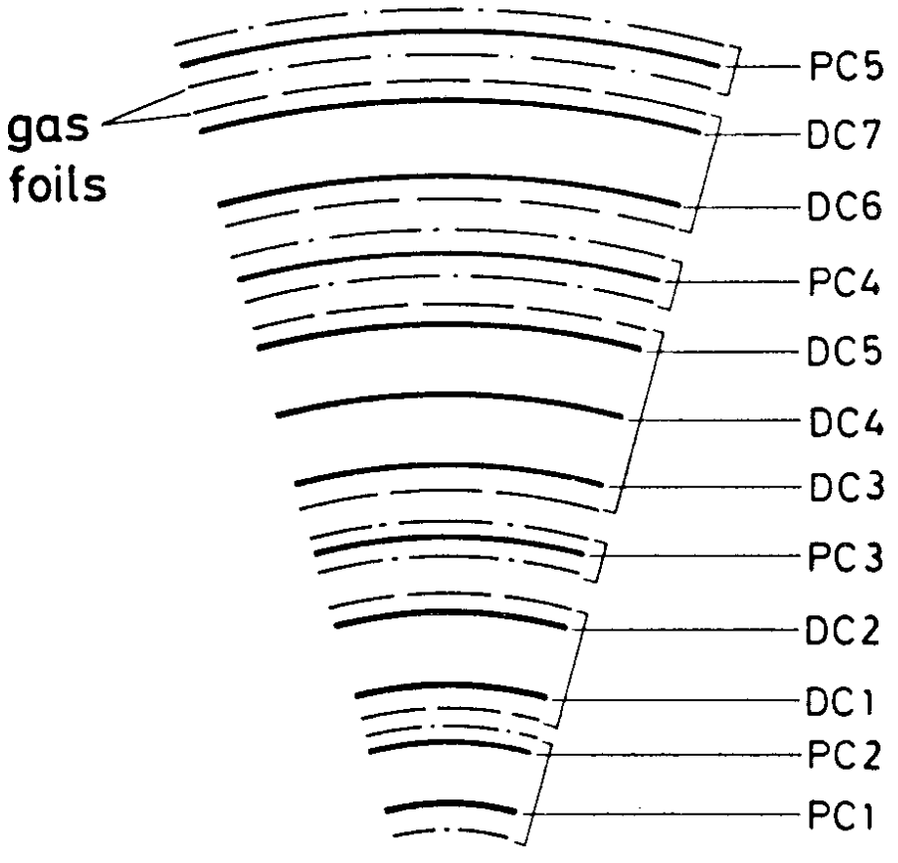
gas
foils
PC5
DC7
DC6
PC4
DC5
DC4
DC3
PC3
DC2
DC1
PC2
PC1

Fig. 2

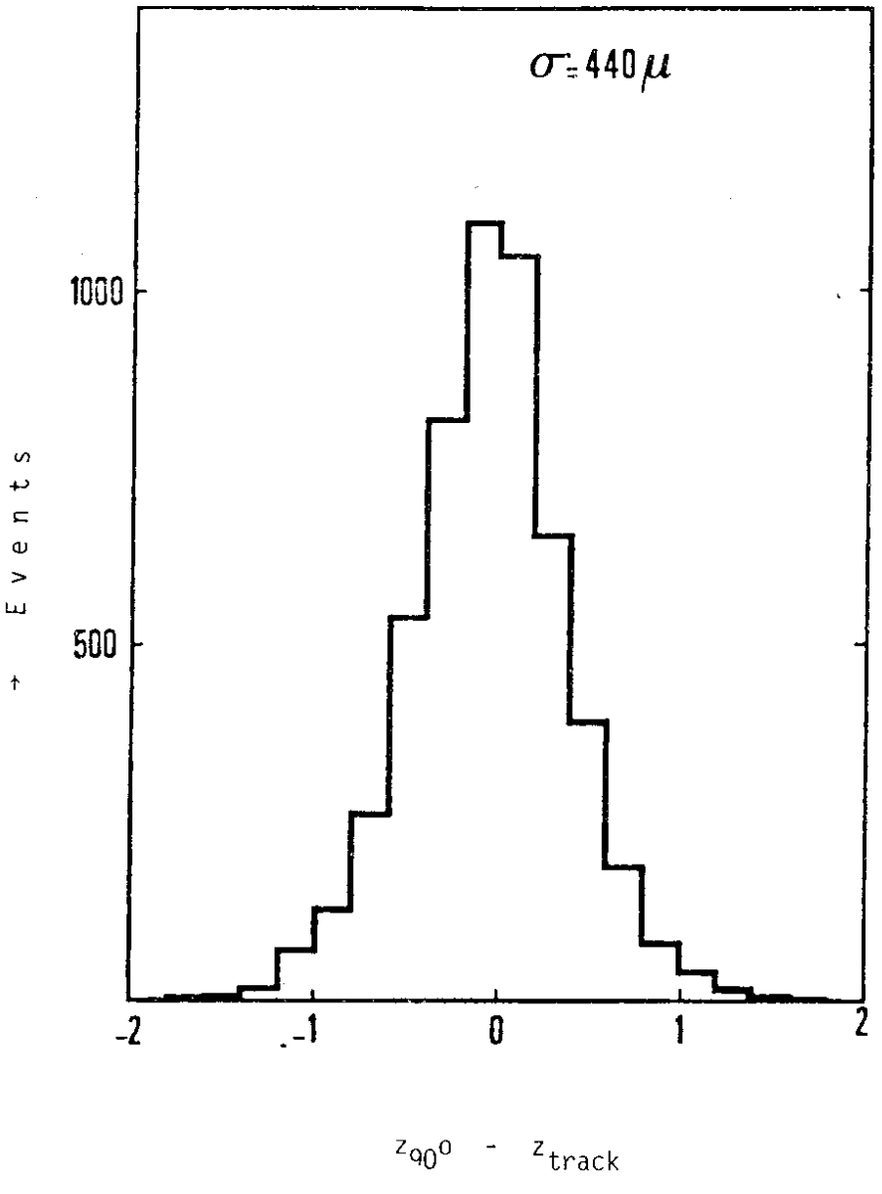
σ = 440 μ
1000
500
→ Events
-2
-1
0
1
2
$z_{90^0} - z_{track}$

Fig. 3

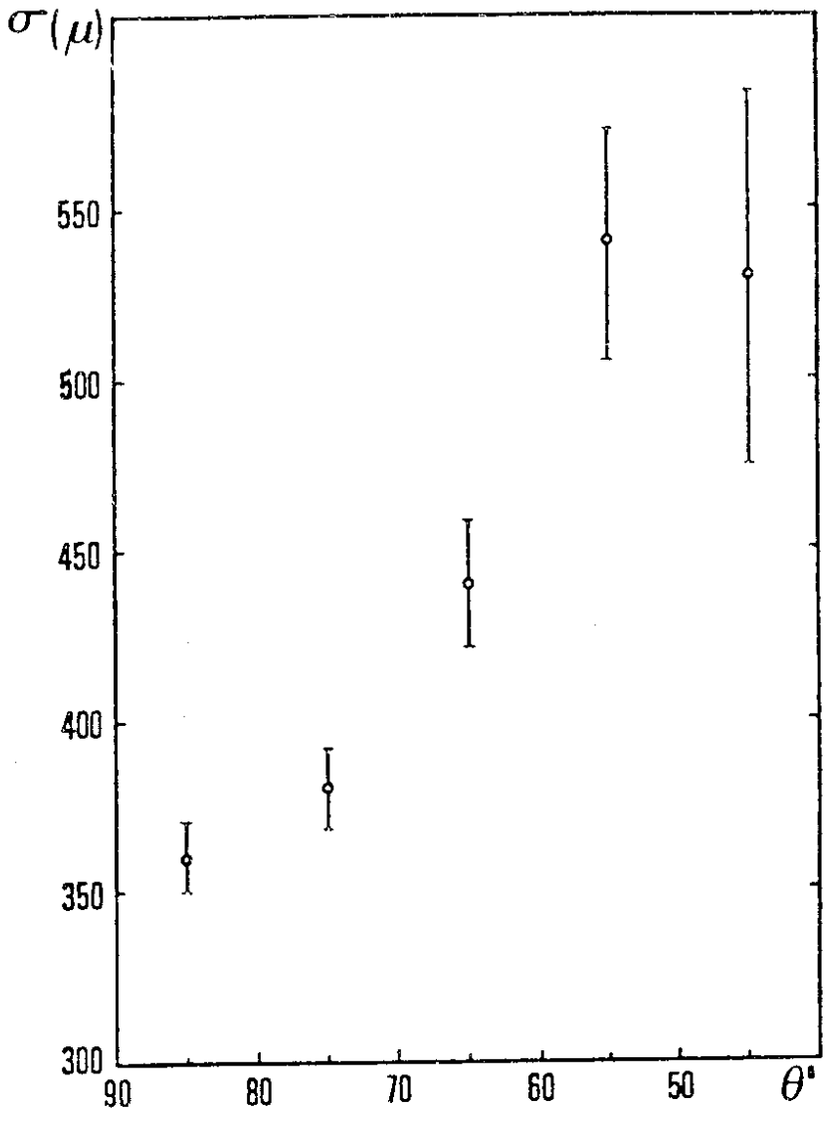
σ(μ)
550
500
450
400
350
300
90
80
70
60
50
θ°

Fig. 4

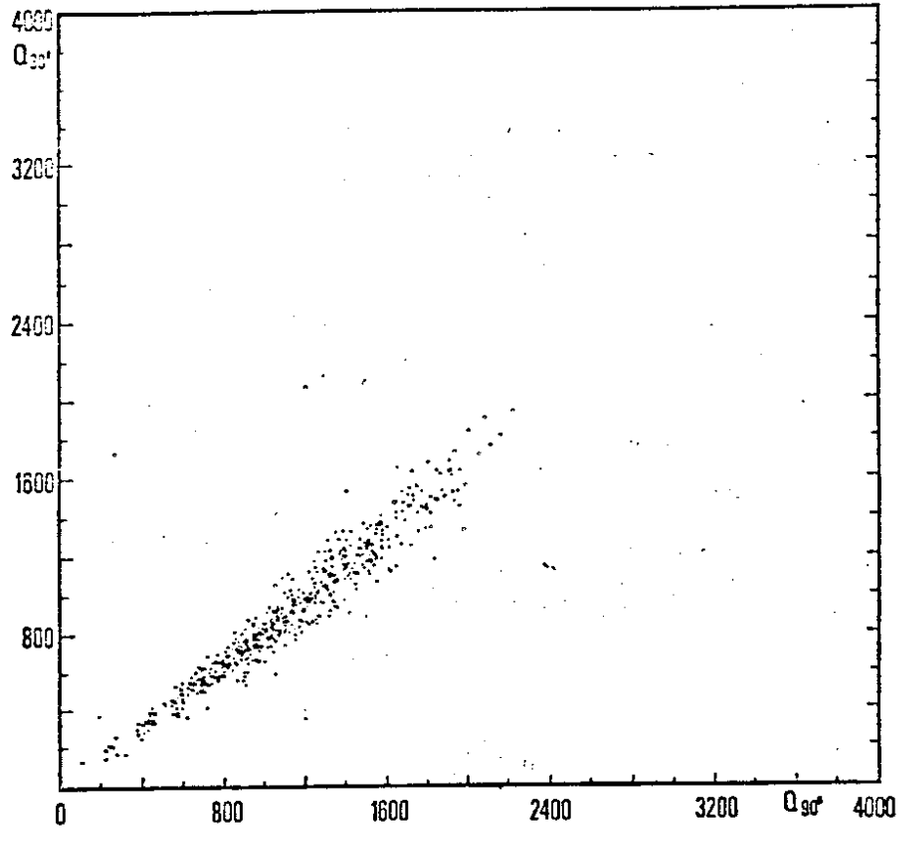
4000
3200
2400
1600
800
0
800
1600
2400
3200
4000

Fig. 5

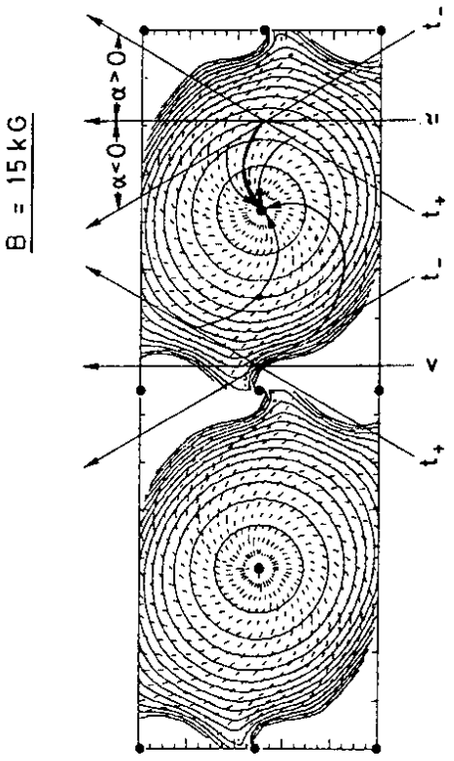

Fig. 7a

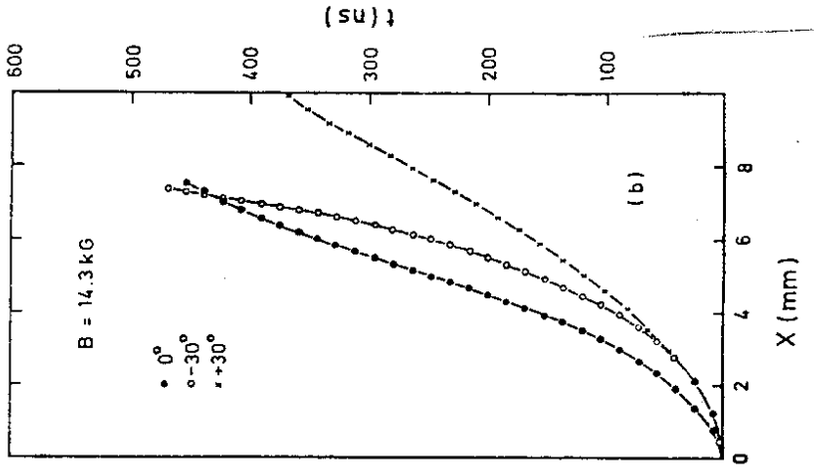

Fig. 7b

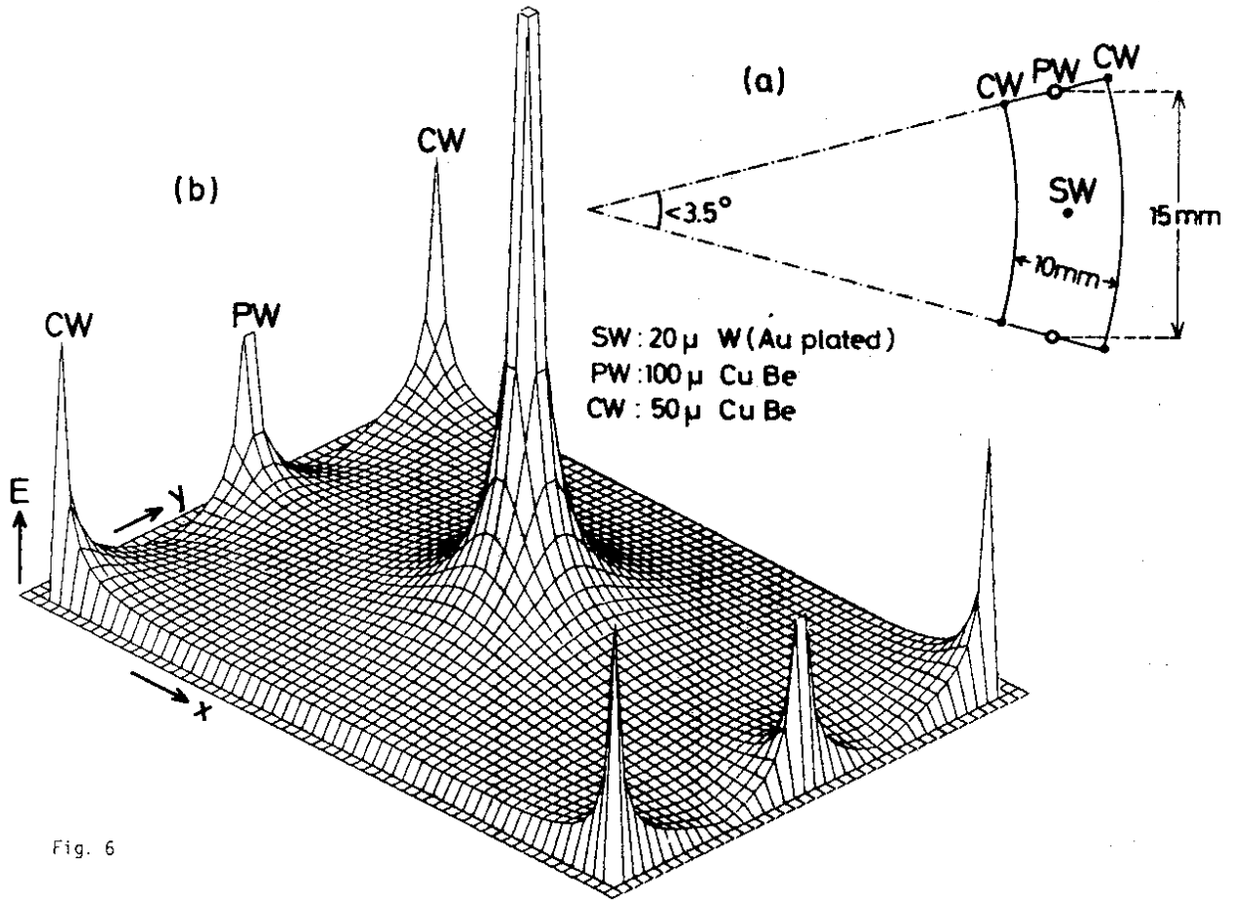

Fig. 6

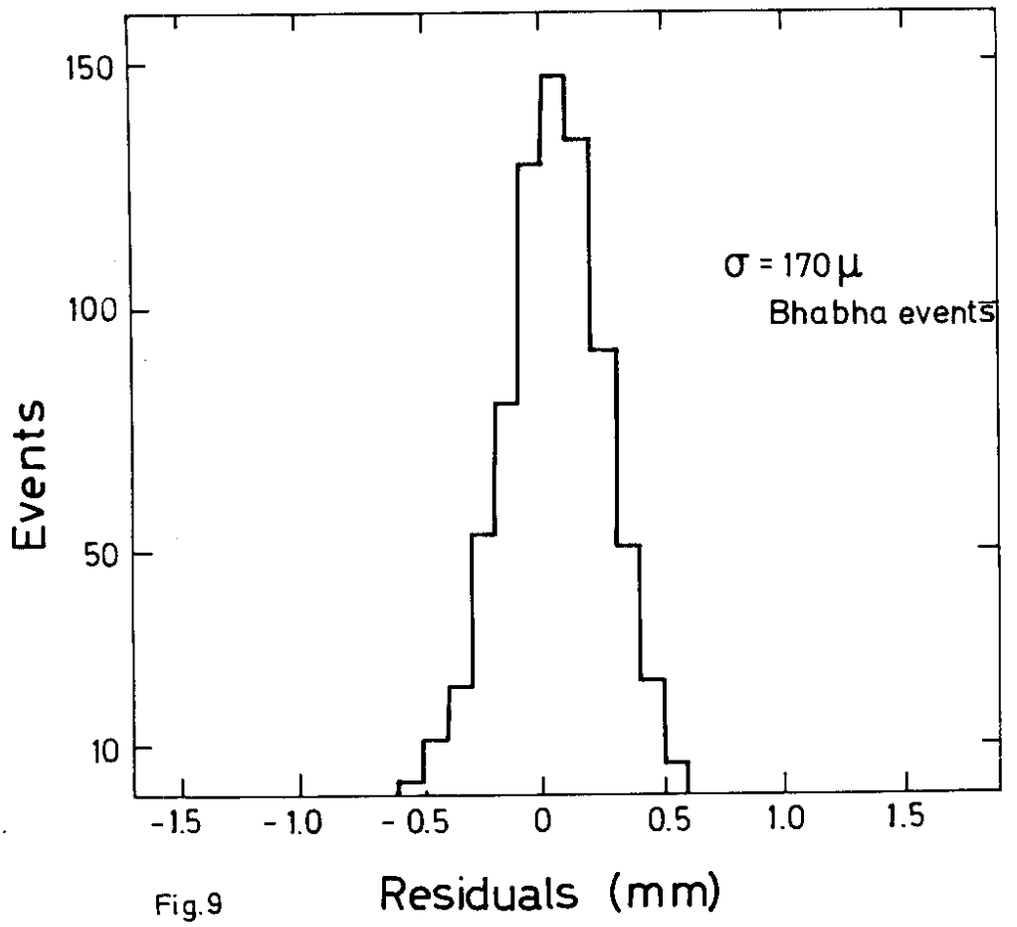

Fig.9

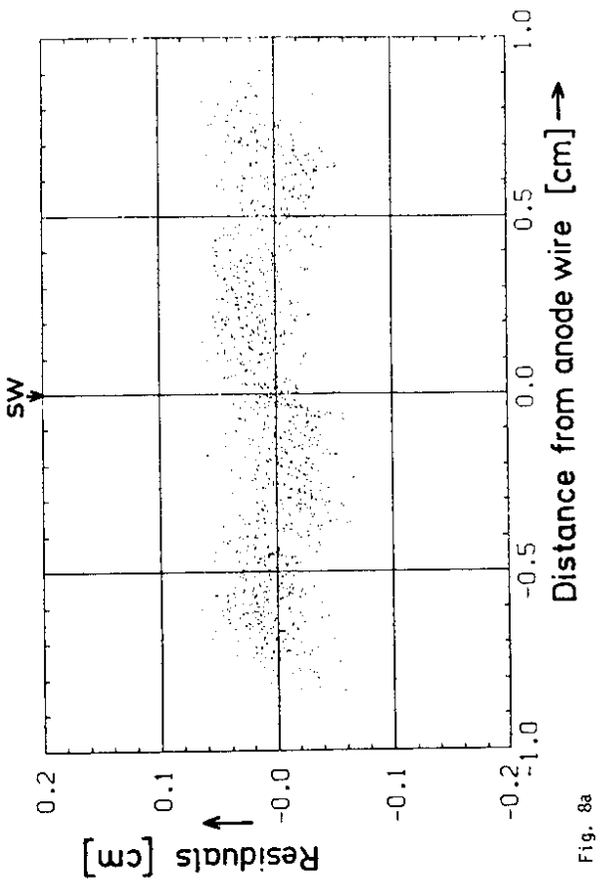

Fig. 8a

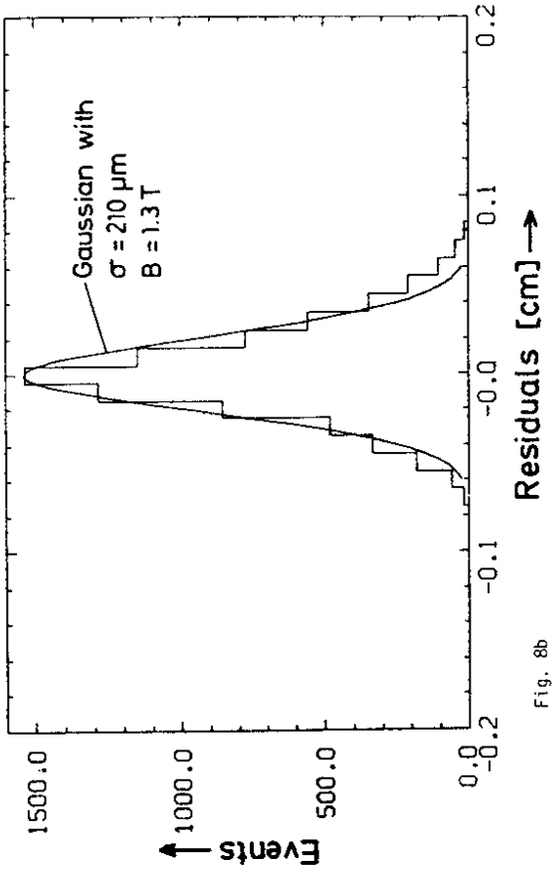

Fig. 8b

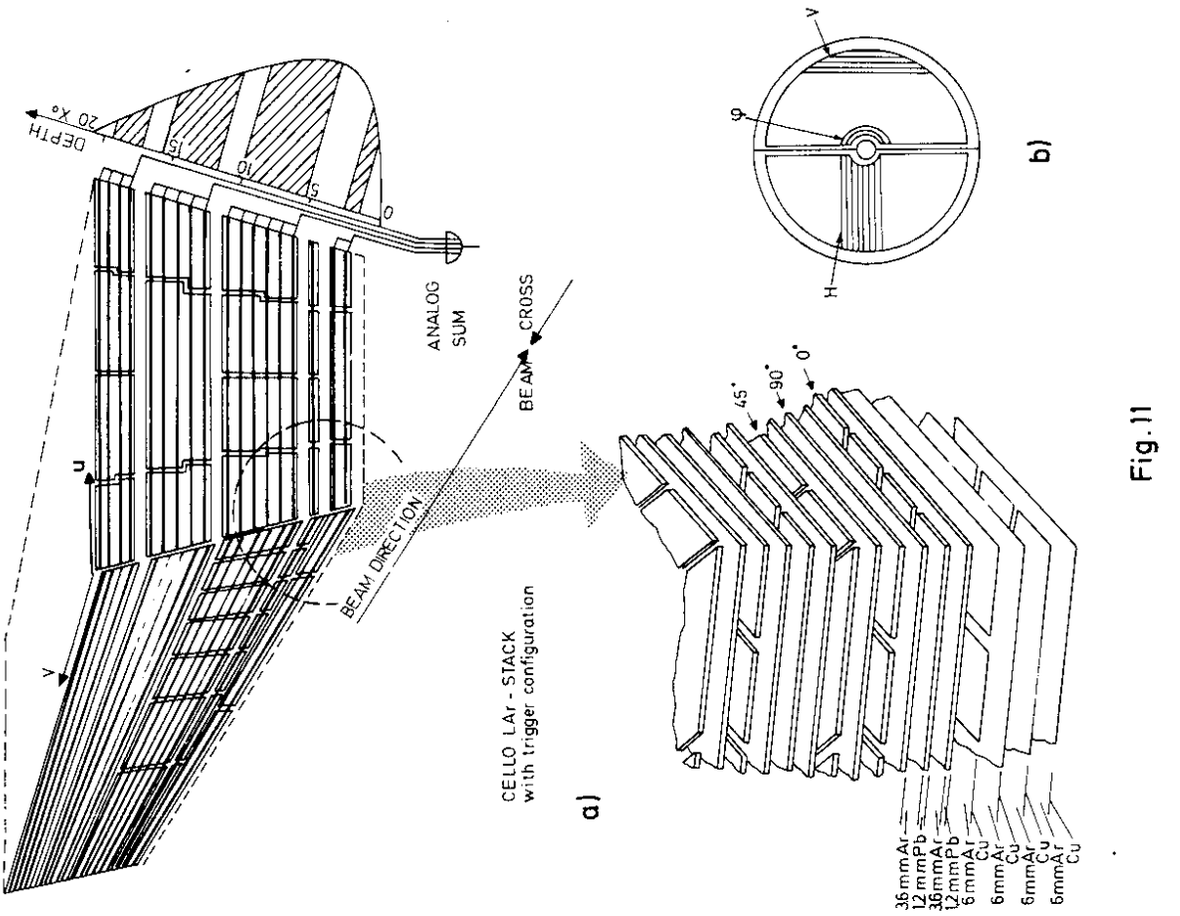

Fig. 11

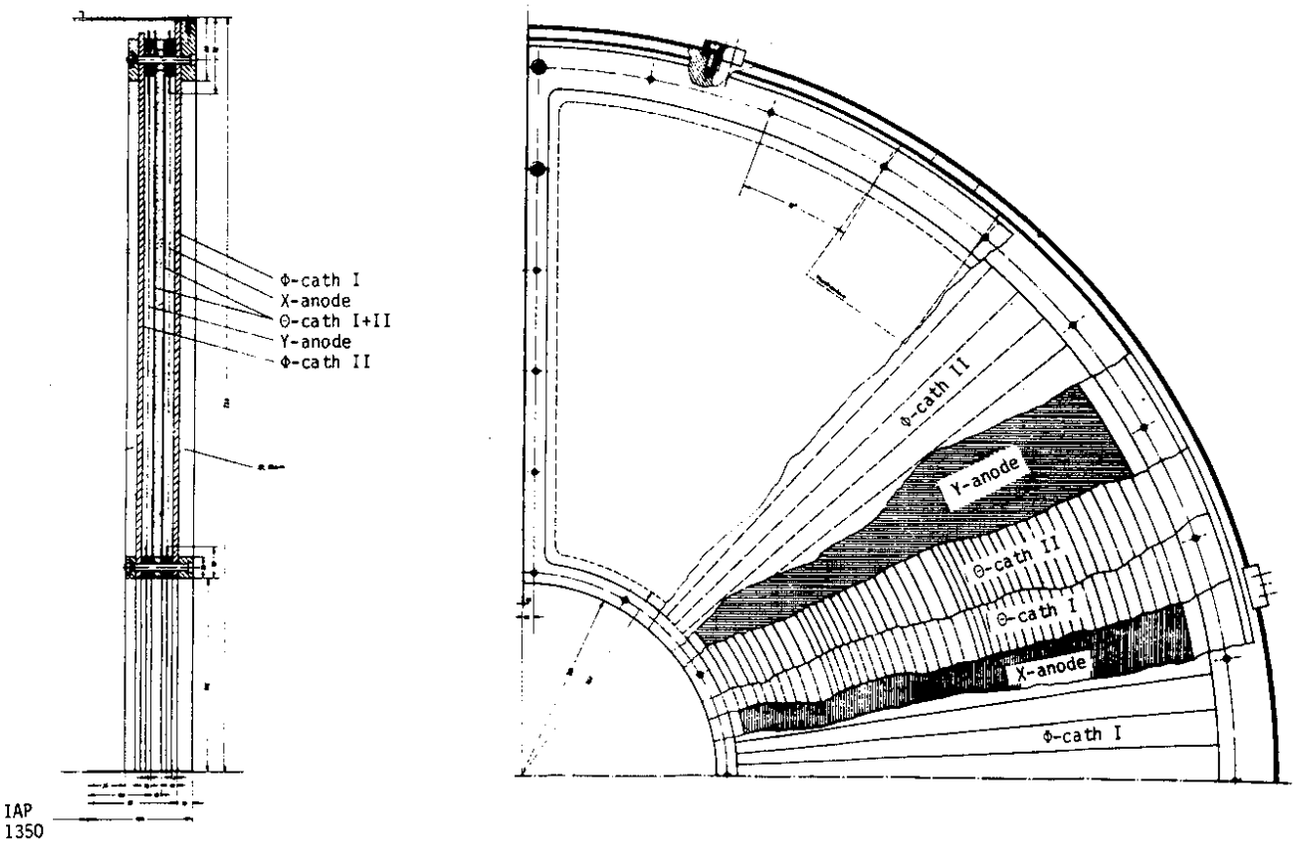

Fig. 10: Layout of the Endcap Multiwire Proportional Chambers

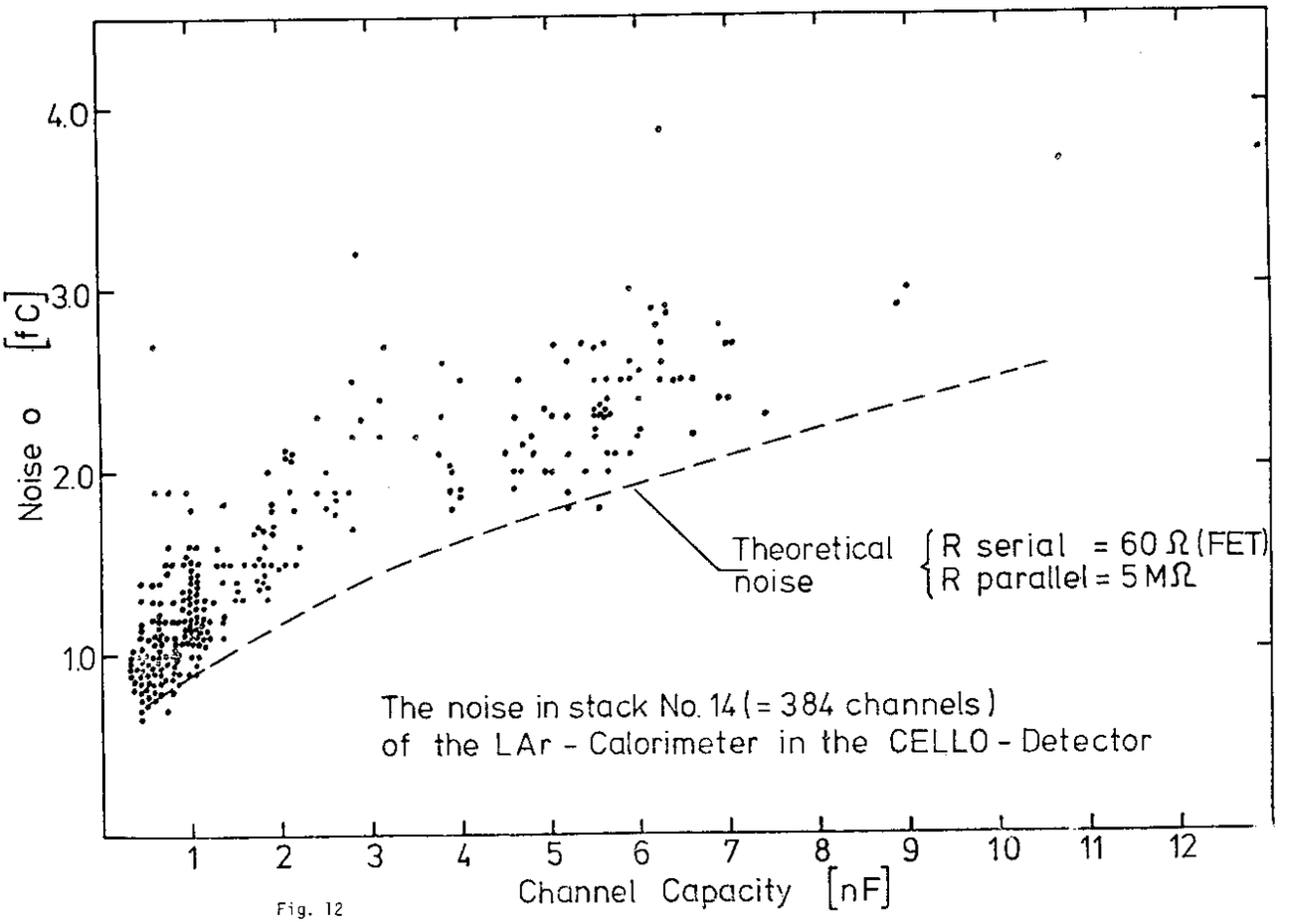

Fig. 12

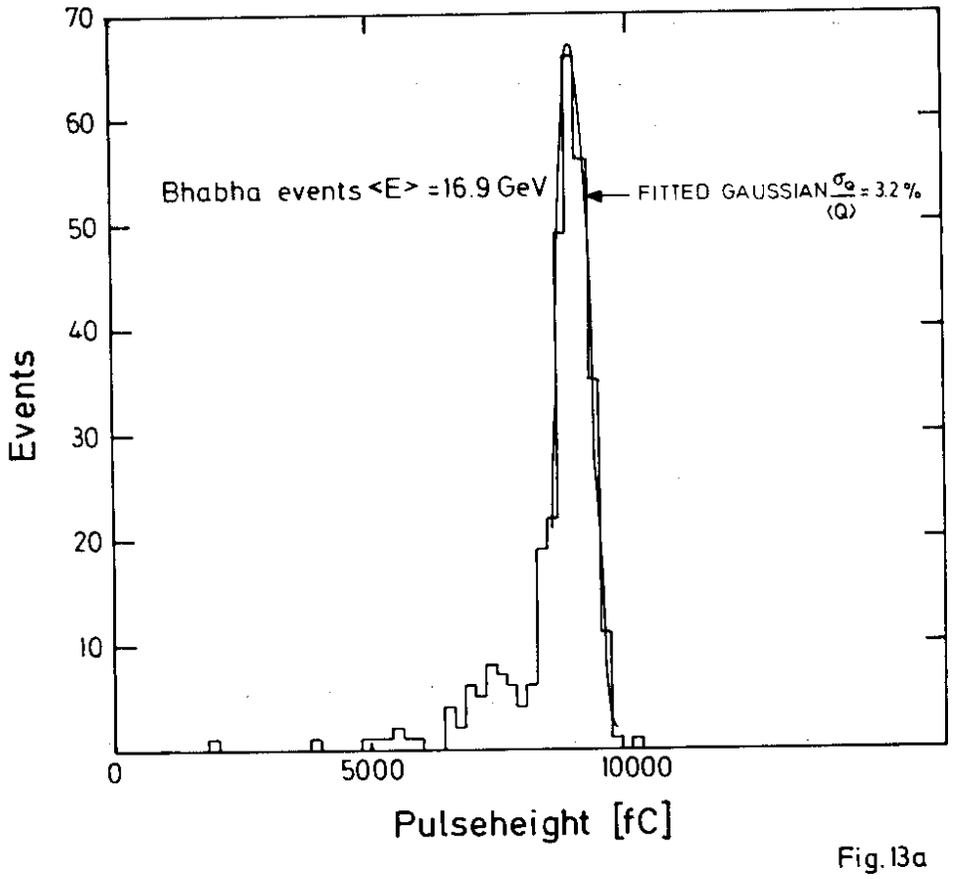

Fig. 13a

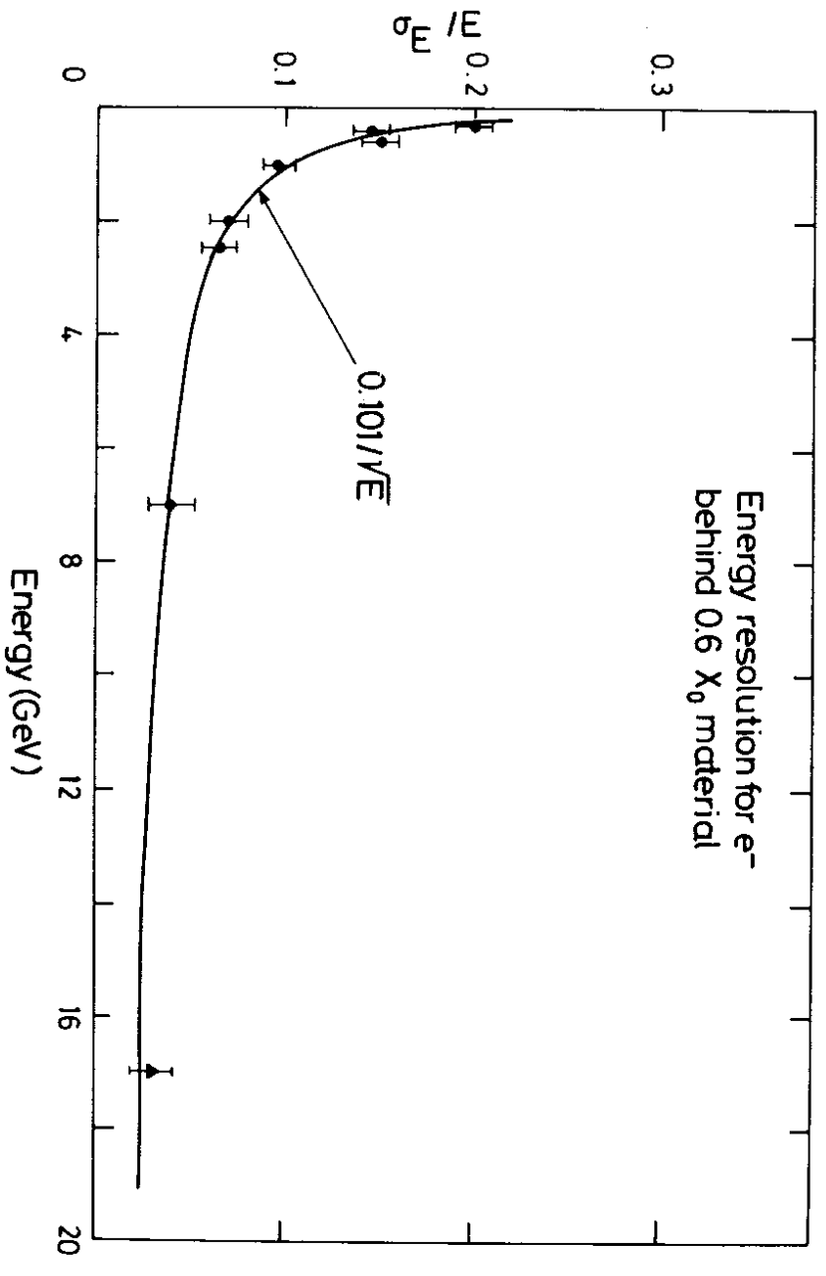

Fig 13b

X-Y-R Correlation

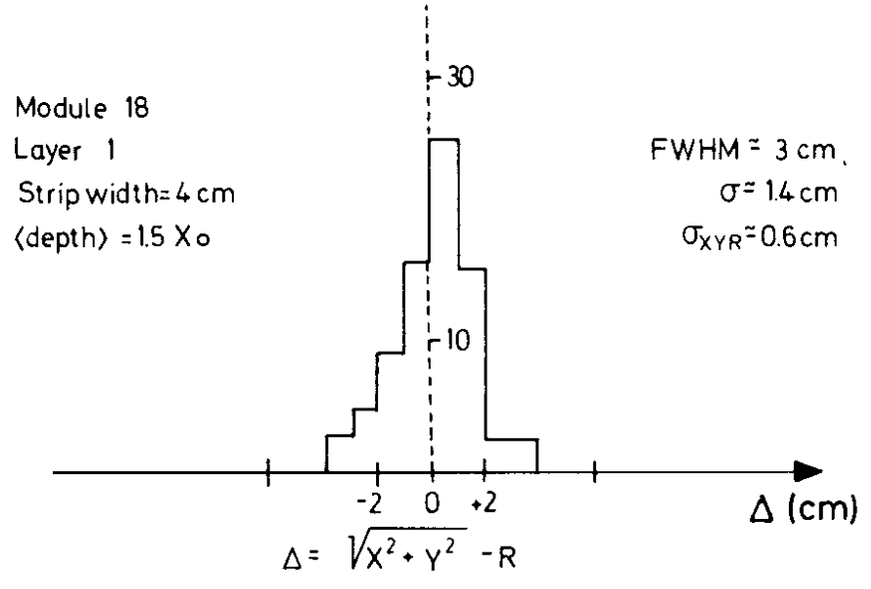

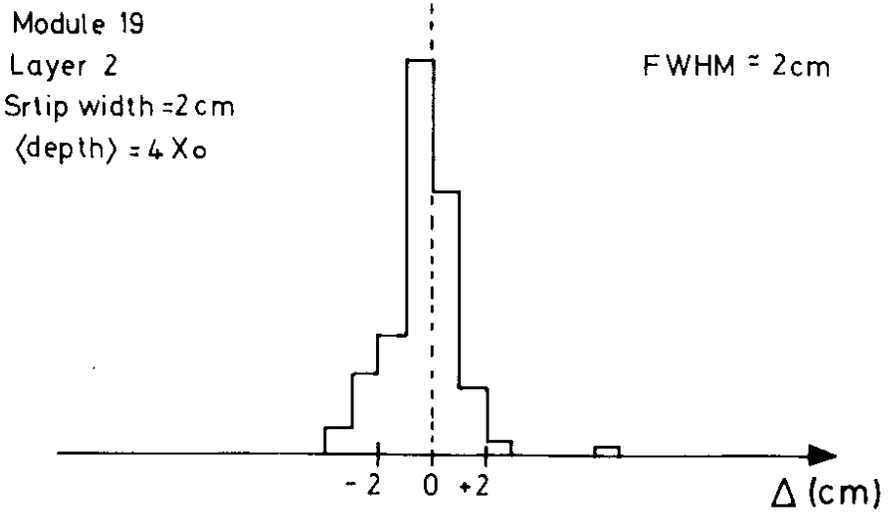

Fig.14

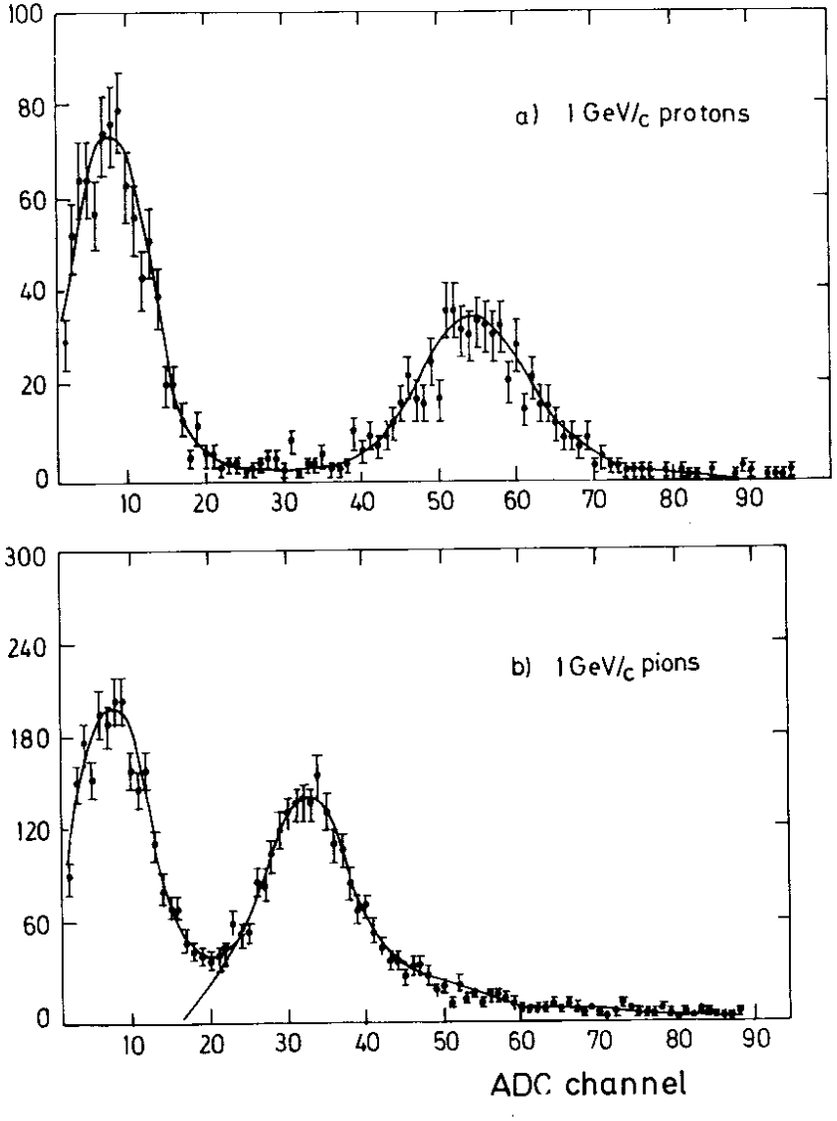

Fig 15

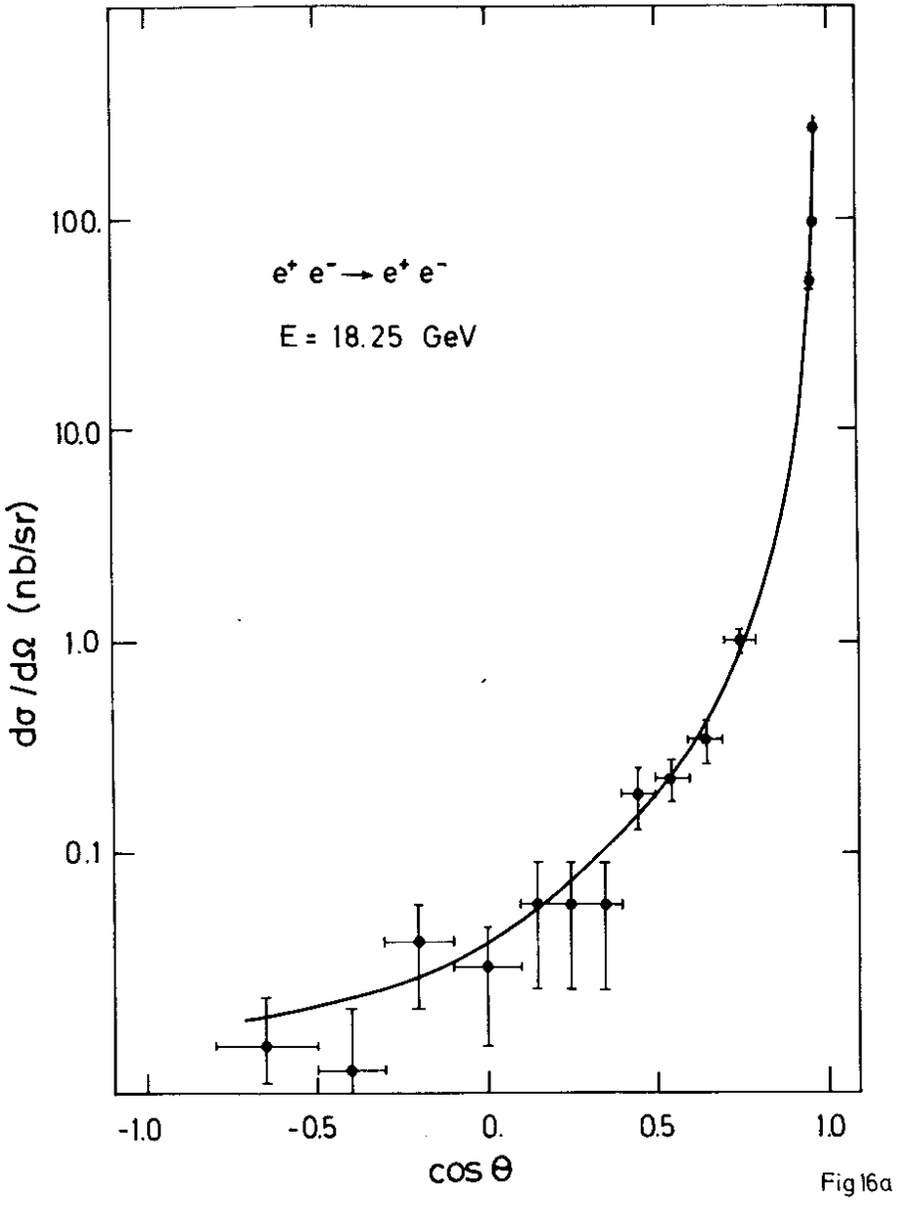

Fig 16a

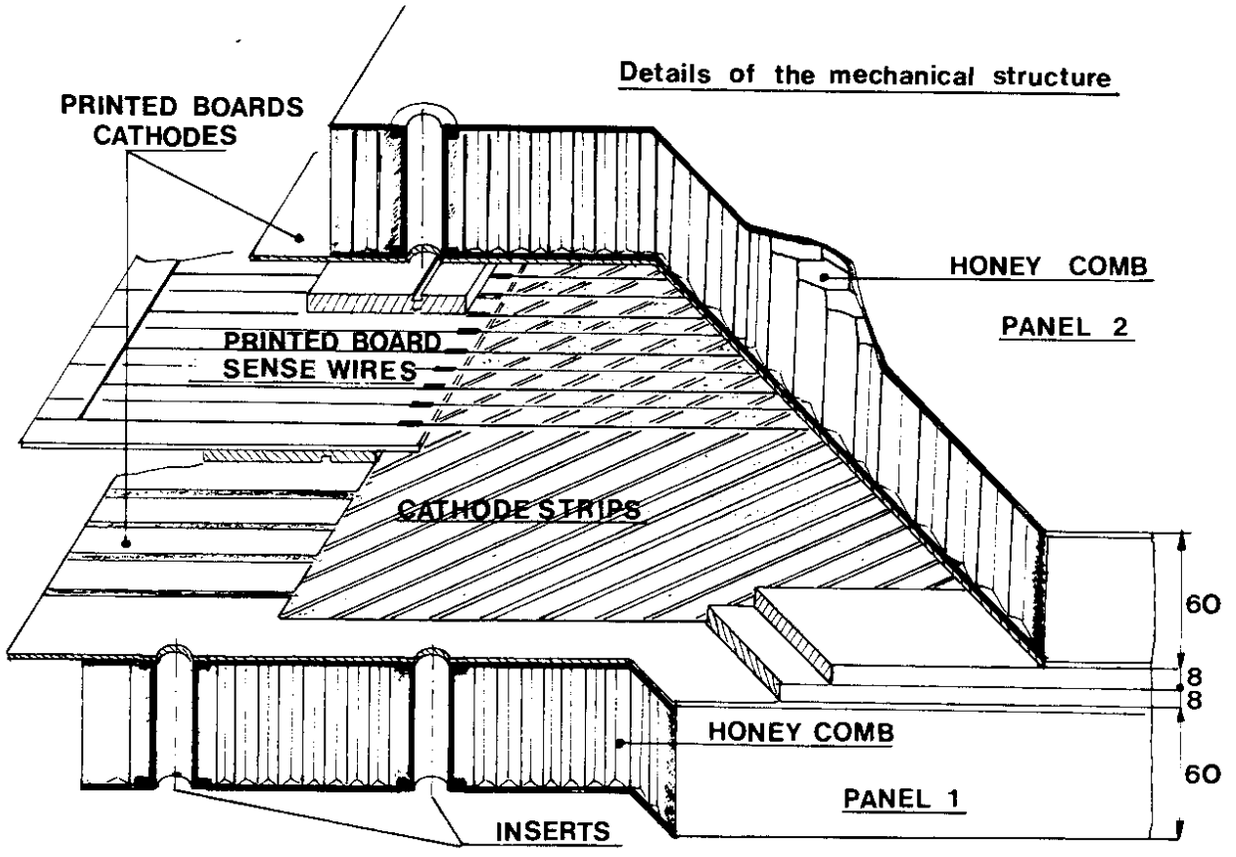

Fig. 17

Fig 16 b

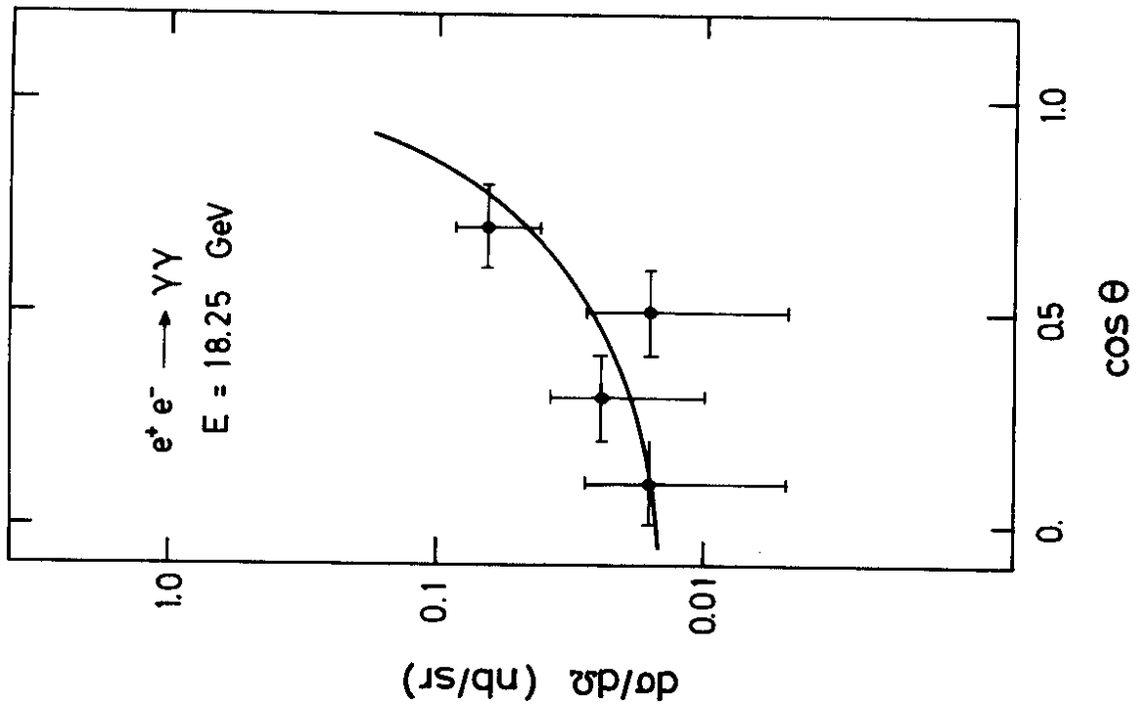

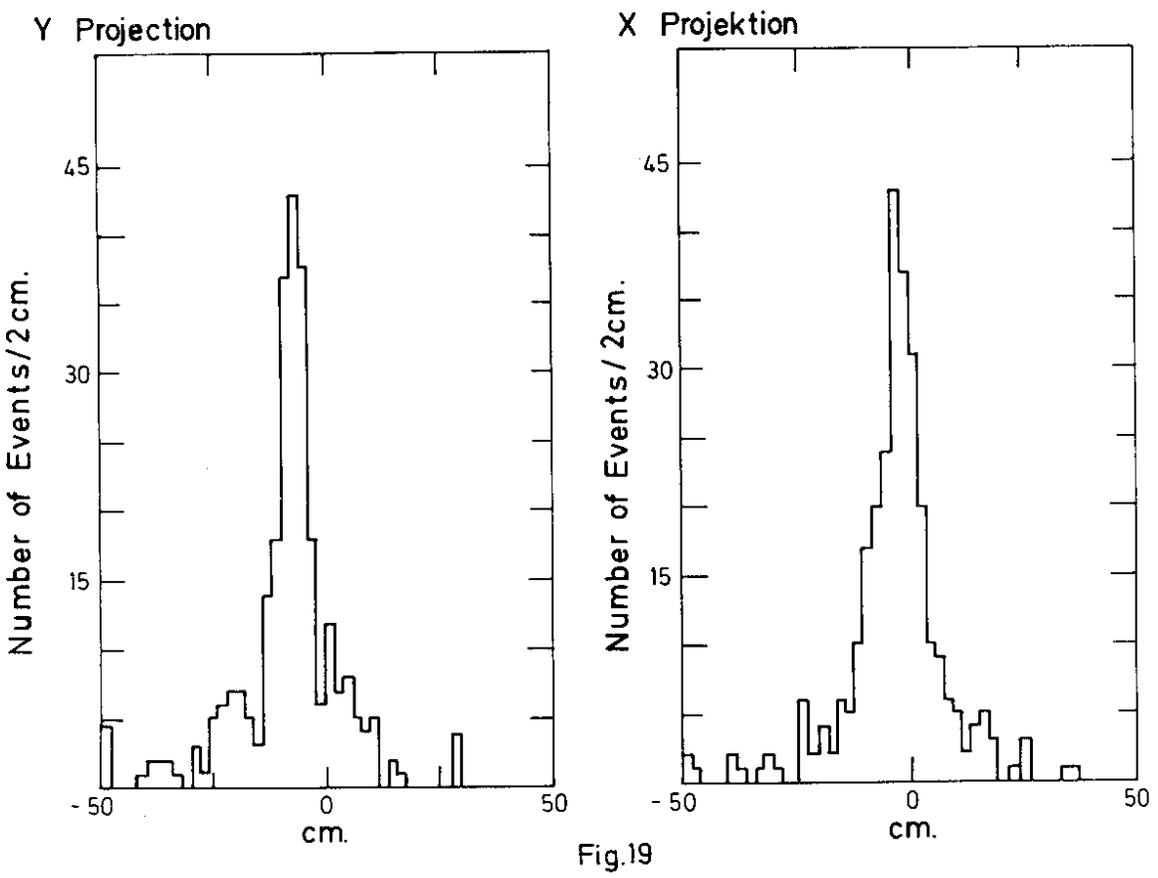
μ Chamber # 7
Y Projection
X Projektion
Number of Events/2cm.
45
30
15
-50
0
50
cm.

Fig.19

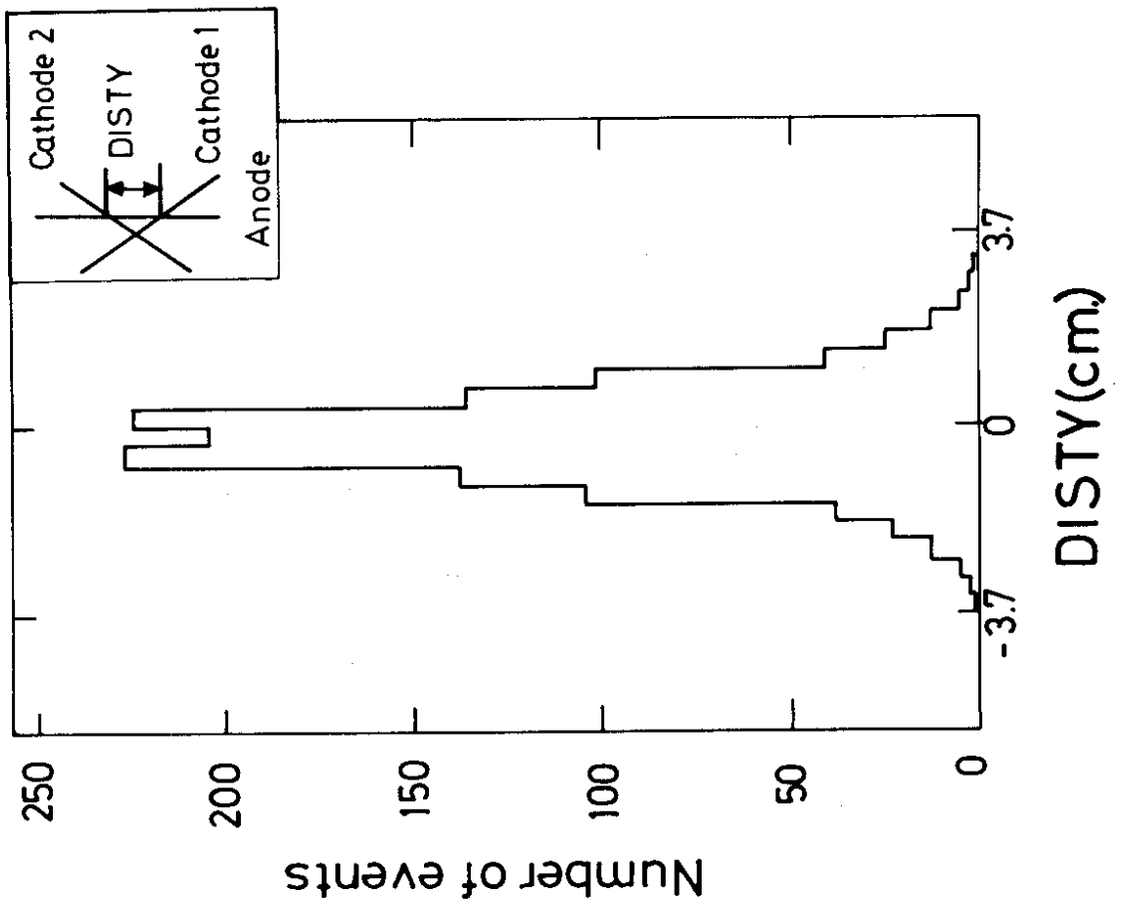
Cathode 2
DISTY
Cathode 1
Anode
Number of events
250
200
150
100
50
0
3.7
0
-3.7
DISTY(cm)

Fig.18

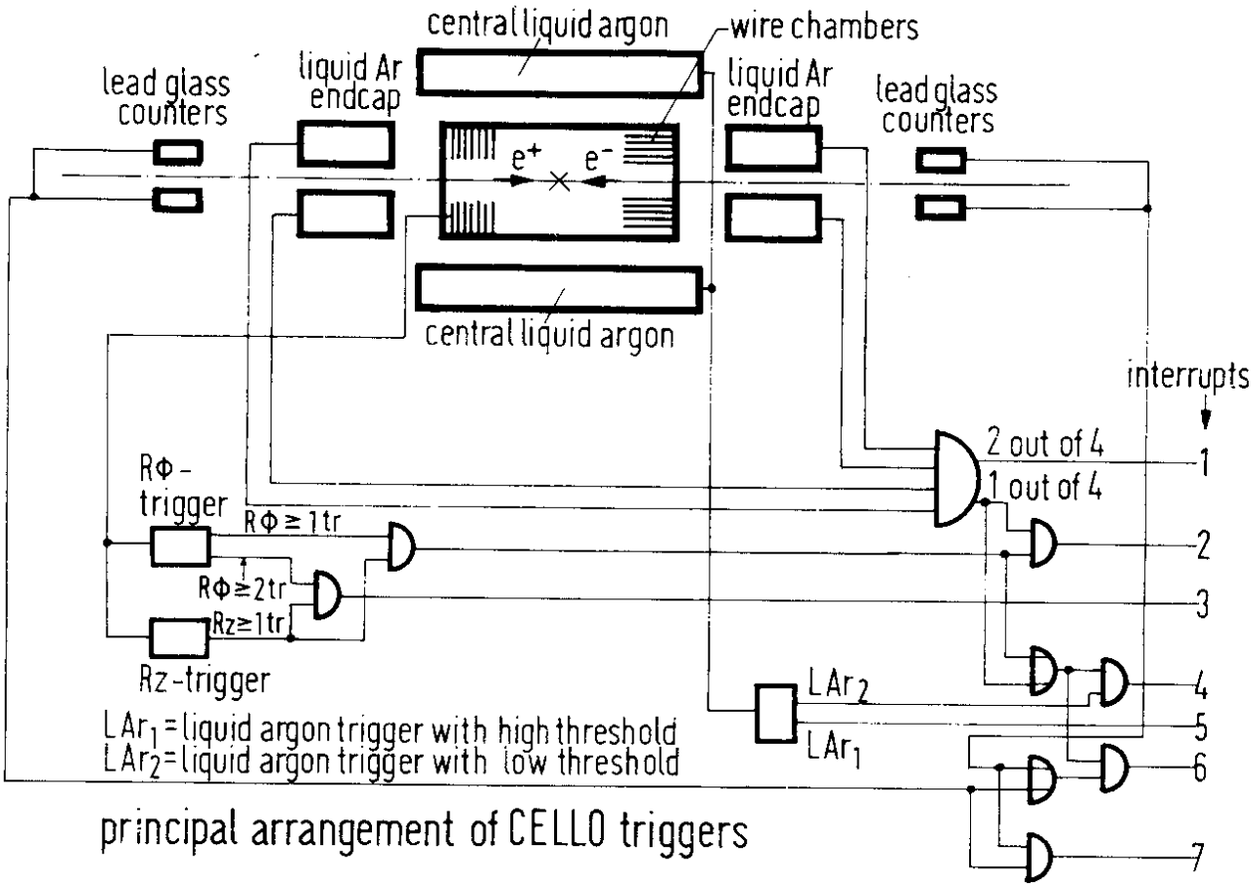

principal arrangement of CELLO triggers

Fig. 21

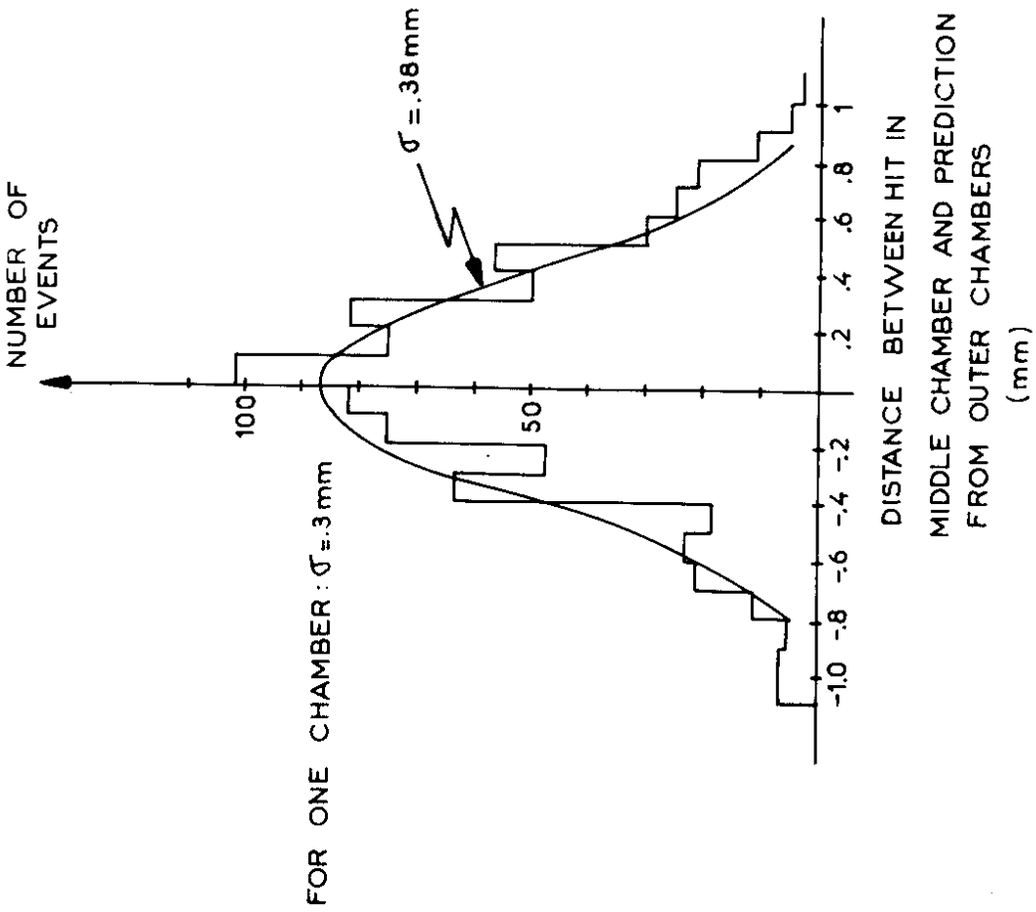

Fig.20

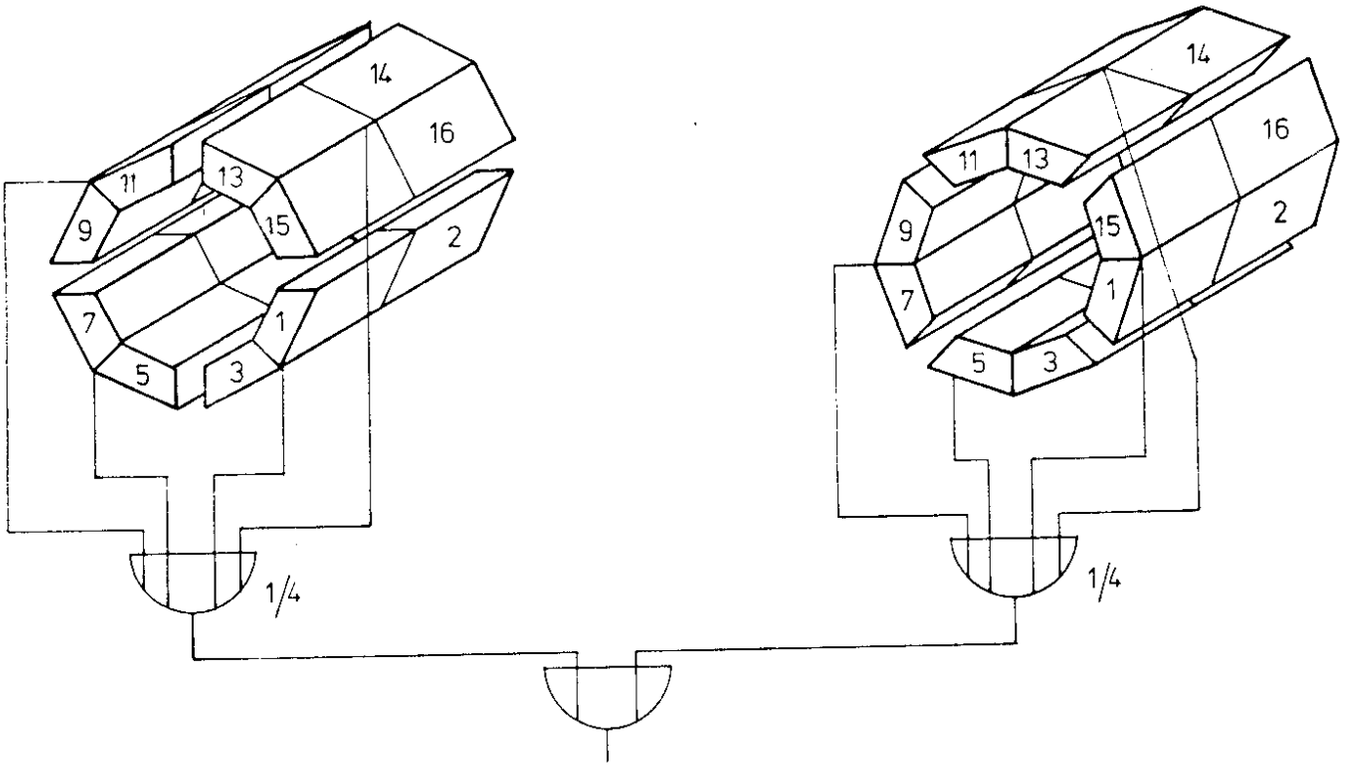

Liquid Argon Trigger

Fig. 22

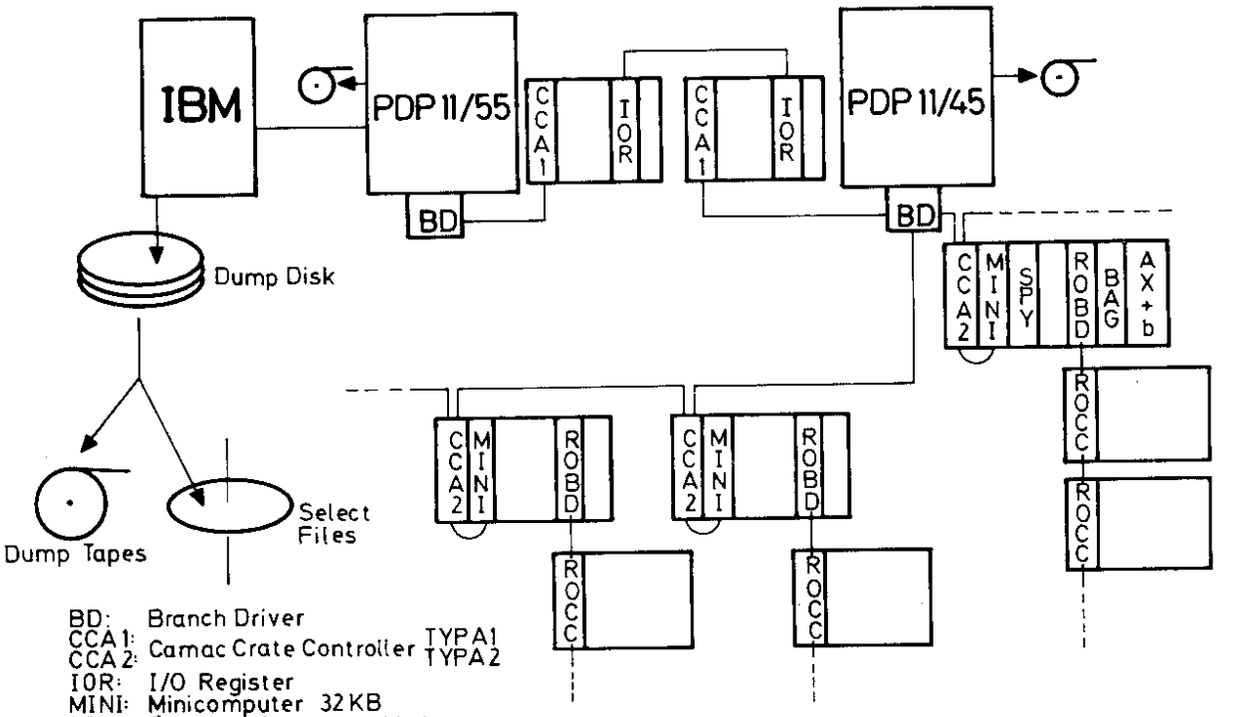

BD: Branch Driver
CCA1: Camac Crate Controller TYPA1
CCA2: Camac Crate Controller TYPA2
IOR: I/O Register
MINI: Minicomputer 32 KB
SPY: Dataway Access by Mini
BAG: Block Address Generator
AX+b: Transform Digital Readout to Physical Units
ROBD: Romulus Branch Driver
ROCC: Romulus Crate Controller

Fig 23

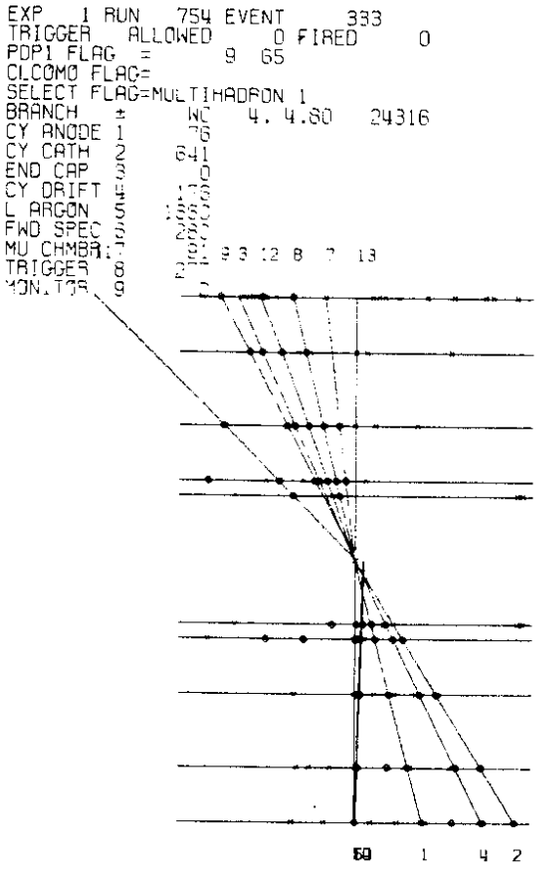
EXP 1 RUN 754 EVENT 333
TRIGGER ALLOWED 0 FIRED 0
PDP1 FLAG = 9 65
CLCOMO FLAG=
SELECT FLAG=MULTIHADRON 1
BRANCH ± NC 4. 4.80 24316
CY ANODE 1 76
CY CATH 2 641
END CAP 3 0
CY DRIFT 4
L ARGON 5
FWD SPEC 6
MU CHMBR 7
TRIGGER 8
MONITOR 9

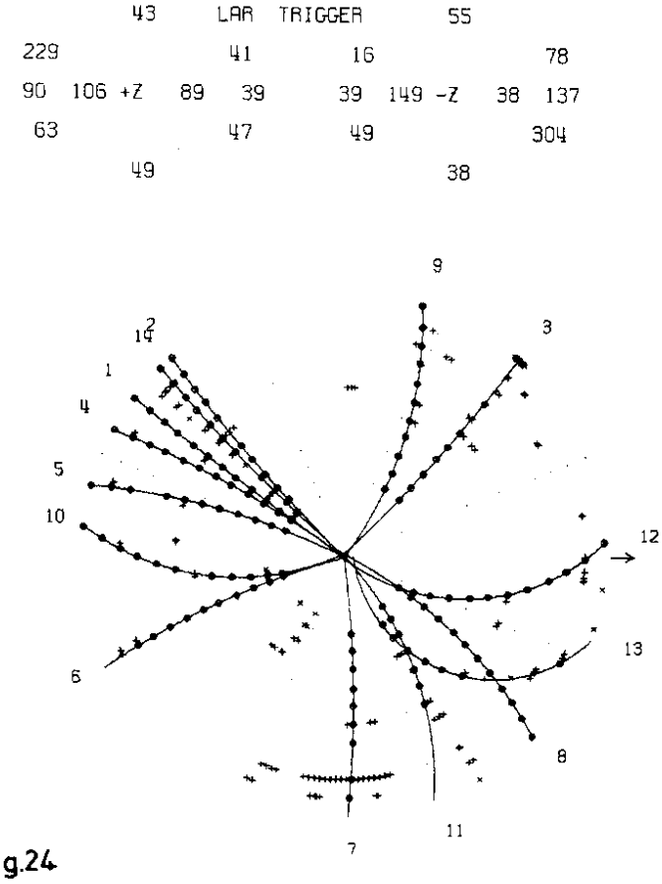
43 LAR TRIGGER 55
229 41 16 78
90 106 +Z 89 39 39 149 -Z 38 137
63 47 49 304
49 38

Fig.24

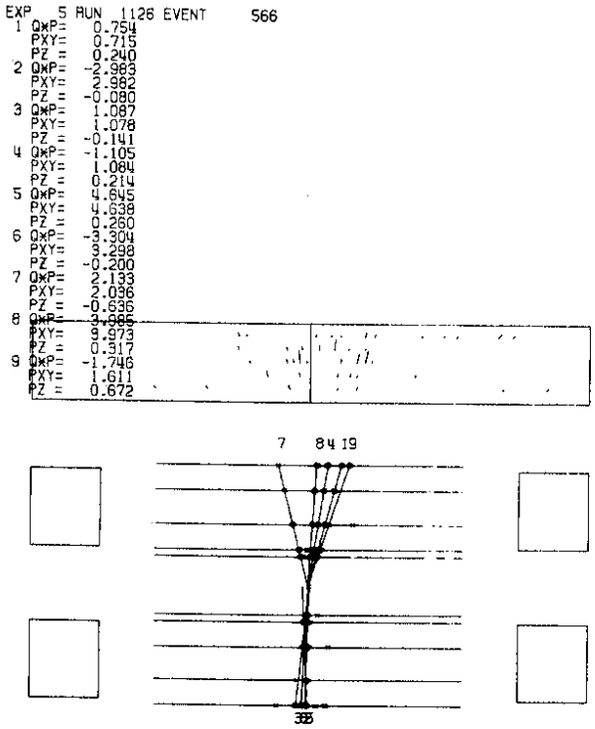
EXP 5 RUN 1126 EVENT 566
1 QxP= 0.754
PXY= 0.715
PZ = 0.240
2 QxP= -2.983
PXY= 2.982
PZ = -0.080
3 QxP= 1.087
PXY= 1.078
PZ = -0.141
4 QxP= -1.105
PXY= 1.084
PZ = 0.214
5 QxP= 4.645
PXY= 4.638
PZ = 0.260
6 QxP= -3.304
PXY= 3.298
PZ = -0.200
7 QxP= 2.133
PXY= 2.096
PZ = -0.636
8 QxP= -3.985
PXY= 3.973
PZ = 0.317
9 QxP= -1.746
PXY= 1.611
PZ = 0.672

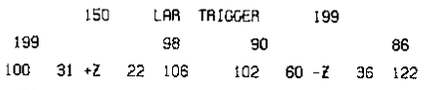
150 LAR TRIGGER 199
199 98 90 86
100 31 +Z 22 106 102 60 -Z 36 122
96 115 86 207
95 90

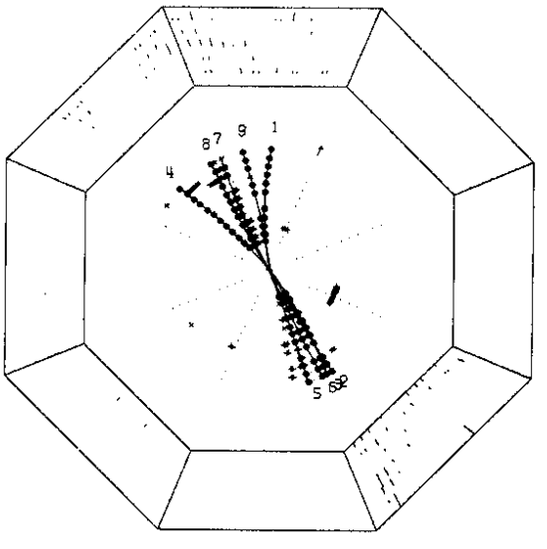

Fig.25

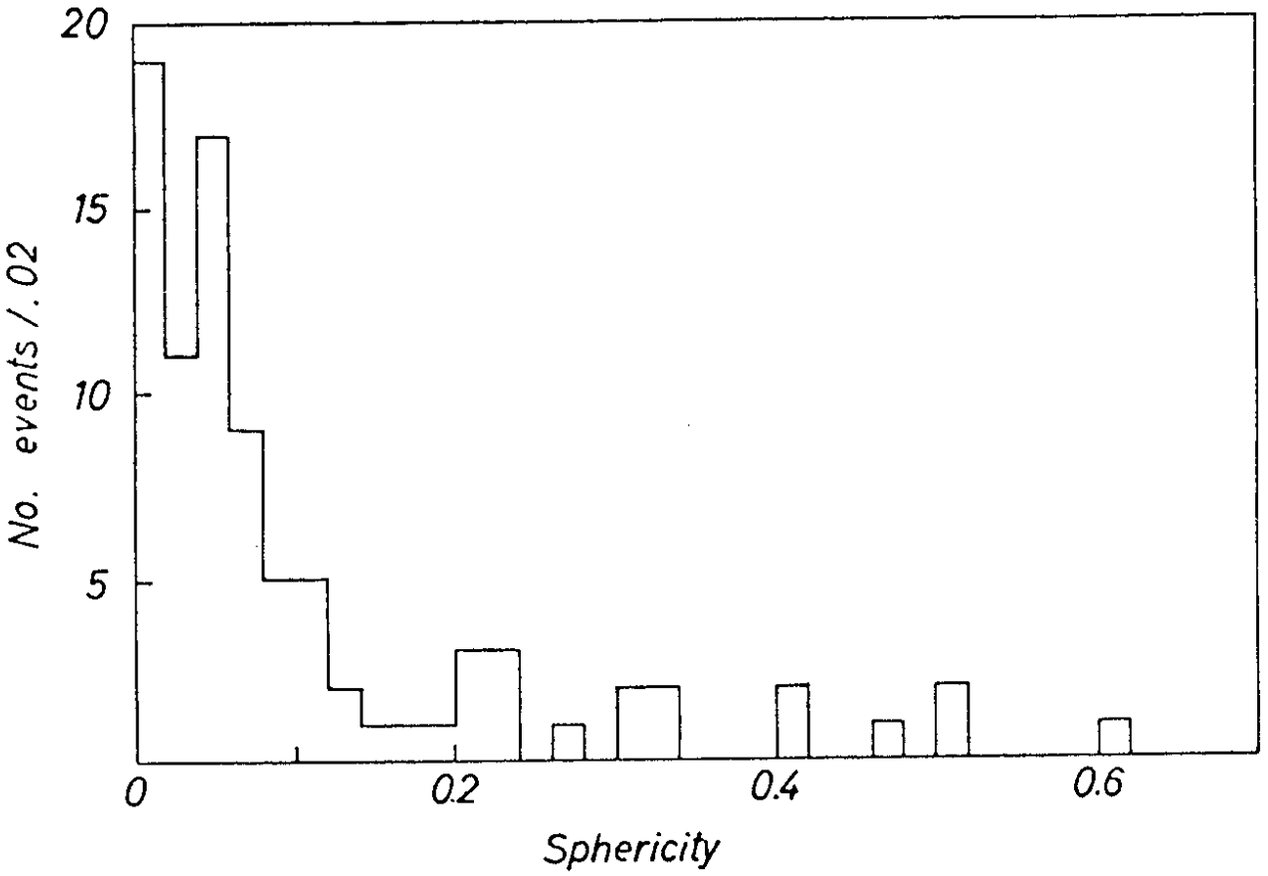
20
15
10
5
No. events / .02
0
0.2
0.4
0.6
Sphericity

Fig.26

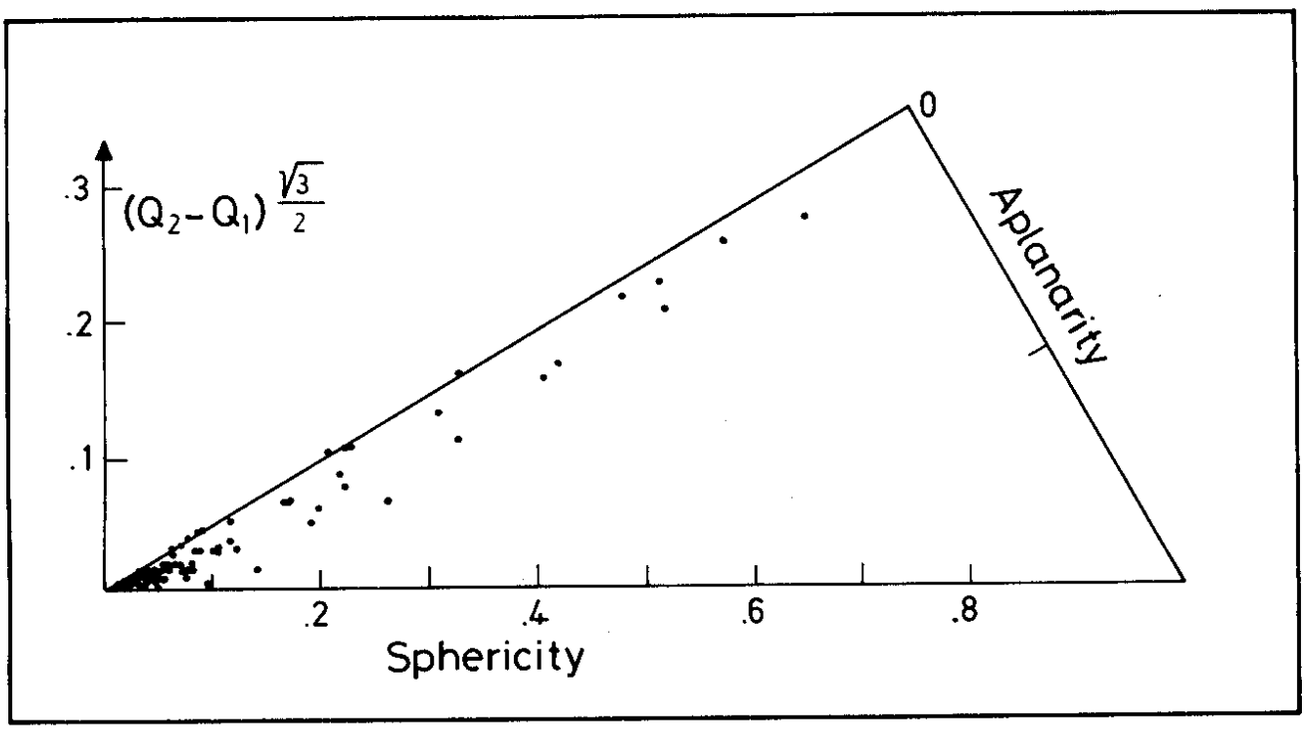
0
Aplanarity
.3
.2
.1
$(Q_2-Q_1)\frac{\sqrt{3}}{2}$
.2
.4
.6
.8
Sphericity

Fig. 27